# Impact of Channel Geometry and Rotation on the Trapping of Internal Tides

SYBREN DRIJFHOUT

*Royal Netherlands Meteorological Institute (KNMI), De Bilt, Netherlands*

LEO R. M. MAAS

*Royal Netherlands Institute for Sea Research (NIOZ), Texel, Netherlands*

(Manuscript received 29 March 2006, in final form 14 February 2007)

ABSTRACT

The generation and propagation of internal tides has been studied with an isopycnic three-dimensional ocean model. The response of a uniformly stratified sea in a channel, which is forced by a barotropic tide on its open boundary, is considered. The tide progresses into the channel and forces internal tides over a continental slope at the other end. The channel has a length of 1200 km and a width of 191.25 km. The bottom profile has been varied. In a series of four experiments it is shown how the cross-channel geometry affects the propagation and trapping of internal tides, and the penetration scale of wave energy, away from the continental slope, is discussed. In particular it is found that a cross-channel bottom slope constrains the penetration of the internal tidal energy. Most internal waves refract toward a cross-channel plane where they are trapped. The exception is formed by edge waves that carry part of the energy away from the continental slope. In the case of rotation near the continental slope, the Poincaré waves that arise in the absence of a cross-channel slope no longer bear the characteristics of the wave attractor predicted by 2D theory, but are almost completely arrested, while the right-bound Kelvin wave preserves the 2D attractor in the cross-channel plane, which is present in the nonrotating case. The reflected, barotropic right-bound Kelvin wave acts as a secondary internal wave generator along the cross-channel slope.

## 1. Introduction

Near rough-bottom topography the turbulent mixing that is associated with the breaking of internal waves contributes about half of the mixing that is required to maintain the large-scale meridional overturning circulation in the ocean (Munk and Wunsch 1998; Wunsch and Ferrari 2004). These internal waves are generated by flow over the topography; in the deep ocean, the most important source is the barotropic tide. Egbert and Ray (2001) examined the tidal dissipation by comparing models for the global barotropic tide and the Ocean Topography Experiment (TOPEX)/Poseidon altimetry data. It appeared that most tidal energy was lost at locations where the currents were perpendicular to the topography, in agreement with the mechanism for internal tide generation.

Internal wave theory suggests that less than 30% of the associated energy flux is generated at small spatial scales that may dissipate locally (St. Laurent and Garrett 2002), while the remainder radiates away as low-mode internal tides or in the form of beams (Pingree and New 1989; Morozov 1995; Lam et al. 2004). Topographically enhanced mixing that is driven by the dissipation of internal tides that are locally generated above rough-bottom topography was observed by Polzin et al. (1997). A parameterization for this locally enhanced mixing was suggested by St. Laurent et al. (2002), based on a combination of theoretical and heuristic arguments. The lower modes that radiate away are relatively insensitive to most dissipation mechanisms (St. Laurent and Garrett 2002) and they have been tracked up to 1000 km from their generation site (Ray and Mitchum 1997). As a result the dissipation sites for these waves must be unrelated to their generation site. This is in agreement with the more or less universal internal wave spectrum in the open ocean (Garrett and Munk 1972), and the assumption of a uniform, constant background diffusiv-

*Corresponding author address:* S. Drijfhout, Royal Netherlands Meteorological Institute (KNMI), P.O. Box 201, 3730 AE De Bilt, Netherlands.
E-mail: drijfhou@knmi.nl

DOI: 10.1175/2007JPO3586.1

ity, away from rough topography (St. Laurent et al. 2002).

Reflection of internal tides at slopes and ridges away from their generation site may, however, lead to energy concentration in specific locations (Müller and Liu 2000). The reason for this is that after their generation internal wave beams, propagating downward, maintain their inclination. As a result, upon reflection from a sloping bottom they get focused when the inclination of the reflecting bottom is opposite to that of the wave beam (Phillips 1963). Upon multiple reflections, in two-dimensional (2D) basins, such focusing predicts the concentration of energy on wave attractors (Maas and Lam 1995). Due to wave focusing, in the open ocean hot spots of mixing may occur at places where the dissipation of the internal wave energy flux is unrelated to the local conversion of barotropic to internal tides.

Wave attractors have been observed experimentally in three-dimensional (3D) confined basins for internal gravity waves (Maas et al. 1997) and also for the analogous class of inertial waves (i.e., for waves in a homogeneous, rotating fluid; Maas 2001; Manders and Maas 2003, 2004). Extending the 2D theory to 3D configurations, ray theory suggests that internal wave attractors may still exist (Manders and Maas 2004), but they would coexist with a regular kind of coastal trapped (edge) wave (Maas 2005). The latter seems to explain near-bottom enhancement of internal tides observed near the concave part of the continental slope (Horn and Meincke 1976; Lerczak et al. 2003). In section 2 we will apply this ray approach to the channel geometry that we investigate. In the present study a fully 3D ocean general circulation model is used to study the possible trapping of internal waves and the existence of internal wave attractors in a 3D geometry. The ocean model is configured for a channel geometry with an open boundary on the "oceanward" side and a "continental" slope at the opposite side. The cross-channel bottom profile is varied. The flow is forced by an incoming barotropic tide at the open boundary. While this configuration is thus not able to model the possible trapping of incident internal waves that have been generated elsewhere in the open ocean, its extension to include remotely forced internal waves is conceptually similar and potentially straightforward.

It is the goal of the present study to show in a series of four experiments how channel geometry affects the 3D propagation of internal tides, to discuss the penetration scale of wave energy, away from the continental slope, and to address the effect of rotation on these issues. The results from the numerical model are compared with the 2D theory of Maas and Lam (1995) on geometric focusing of internal waves and with the predictions based on 3D ray theory discussed next.

## 2. Review of wave focusing in confined basins

Historically, internal waves have often been considered as interfacial waves in two-layer or multilayer systems (Gill 1982). Such interfacial waves retain many similarities with surface waves. Similar to surface waves, their horizontal spatial structure is determined by an elliptic (Helmholtz type) equation, which has regular solutions everywhere. However, this classical approach disregards that in continuously stratified fluids internal waves propagate principally beamwise (with a slope $c$) and that their spatial structure satisfies a hyperbolic equation:

$$\frac{\partial^2 \psi}{\partial y^2} - c^2 \frac{\partial^2 \psi}{\partial z^2} = 0, \tag{1}$$

where $\psi$ denotes the streamfunction, and $y$ and $z$ are the horizontal and vertical coordinates of a Cartesian frame of reference. The reflection of a beam from a sloping bottom entails a change of vertical wavenumber and an abrupt change of scale, which ultimately may lead to the singularities within the fluid domain that are typical for these hyperbolic problems. The beamwise propagation of internal waves follows from the dispersion relation that relates frequency to the wavenumber's *direction* and not, as for surface waves, to wavenumber *magnitude* (Maas 2001, 2005). Thus, internal waves that reflect from a sloping boundary may focus or defocus, depending on the relative inclination to that boundary.

In 2D containers having sloping sidewalls a remarkable finding is that focusing always dominates over defocusing. Focusing and defocusing are at best in balance, but never does defocusing prevail (Maas and Lam 1995). The net effect is that internal waves focus their wave energy onto limit points or limit cycles, so-called wave attractors. These attractors are independent of the source location. The focusing and defocusing reflections, as well as the dominance of the former through the establishment of a wave attractor, can be appreciated by considering the fate of a single ray (see Fig. 1a). The 2D fluid domain is bounded by a rigid surface at $z = 0$ and a parabolic bottom, nondimensionally given by $z = -\tau(1 - y^2)$. Here $\tau = A/c$ is a lumped parameter, or nondimensional depth. It presents the ratio of two inclinations. The first is a gross measure of the channel inclination $A = D/L_y$, based on maximum depth $D$ and channel half-width $L_y$. The second represents the slope of the internal wave characteristics:

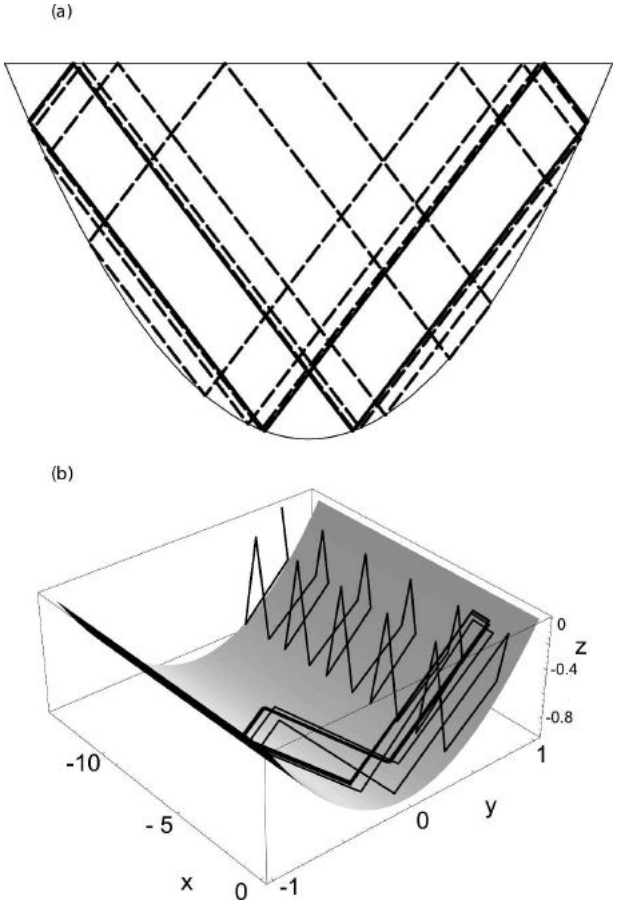


FIG. 1. Ray paths of internal wave beams in a parabolic channel with depth $\tau = 0.94$ starting at the surface. (a) Single ray (dashed) launched at $x = 0$, $y = 0$ toward the right, displaying the appearance of an attractor (solid) in the meridional cross-sectional plane. (b) Two ray paths, both launched at the surface at $x = 0$, $y = 0.75$, one partly cross channel, the other strictly down channel. The former again approaches the wave attractor in the cross-channel plane. The latter propagates oceanward and is stuck to the corridor over the critical slope at $y = 1/(2\tau) = 0.532$.

$$c = \sqrt{\frac{\omega^2 - f^2}{N^2 - \omega^2}}. \tag{2}$$

Here $\omega$ denotes the tidal frequency, $N$ is the stratification rate, and $f$ is the Coriolis frequency. The attractor consists of two rectangles (solid lines) and eventually attracts all rays, which also represent the paths along which the wave energy flux is directed (one example shown as dashed line). This leads to mixing hot spots as the internal wave energy of such focused beams will lead to enhanced shear and internal wave breaking. In real fluids, the intensification is balanced by viscous effects; free internal boundary layers form around the wave attractors (Rieutord et al. 2001; Ogilvie and Lin 2004).

The attractor shape depends fractally on $\tau$ (Maas and Lam 1995). Finite-sized $\tau$ windows, containing large-scale attractors, are interrupted by smaller windows, containing small-scale attractors. Only the former are considered to be physically realizable as the number of boundary reflections needed to cover the small-scale attractors becomes prohibitively large. In the following we choose $\tau$ to reside within the window where the largest-scale attractor lies. Clearly, in any realistic situation one needs to check if any of the relevant tidal frequencies does indeed lie within such a parameter interval before drawing conclusions on its applicability to the internal tide(s).

In the present study, we consider internal tides in a 3D configuration. The internal tides are generated over the continental slope at one end of the channel, and then propagate oceanward. The spatial structure of the internal wave's pressure field is now governed by the 3D Poincaré equation:

$$\frac{\partial^2 p}{\partial x^2} + \frac{\partial^2 p}{\partial y^2} - c^2 \frac{\partial^2 p}{\partial z^2} = 0, \tag{3}$$

where $p$ denotes pressure and $x$ is the dimensionless, along-channel coordinate. The pressure field obeys oblique derivative boundary conditions that prohibit finding exact analytical solutions. In this case some indication of the behavior of the internal waves can be obtained by following individual wave rays. These rays can be locally perceived as representing a plane wave whose path is followed upon multiple reflections from boundaries that are locally approximated as being planar. For any single such reflection Phillips (1963, 1977) solved the reflection problem by computing the changes in wavenumber and amplitude. By applying this ray method in a channel of trapezoidal cross section, Manders and Maas (2004) showed that upon many boundary reflections refraction may lead to down-channel trapping of rays. In a paraboloidal basin, internal wave trapping is accompanied by another, regular type of ray behavior (Maas 2005). It is a quasi-periodic ray structure in which rays hug the critical circle. This circle connects critical points, where the bottom inclination is the same as that of the rays. The ray structure suggests a kind of internal edge wave, similar to the whispering gallery mode in elliptic problems, but now trapped to the critical circle. Applied to the parabolic channel configuration, employed in the present study, we anticipate that successive focusing and defocusing reflections may lead to partial trapping and partial leaking of the internal waves: waves are either attracted to the cross-channel plane, such that they will be trapped at a finite penetration distance from the source, or waves propagate outward by following the waveguide around the critical depth.

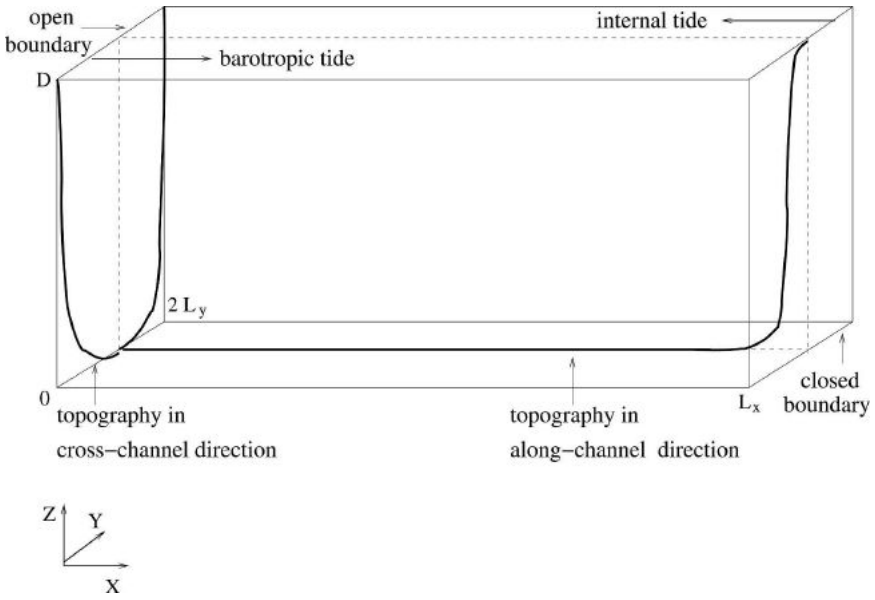


FIG. 2. Schematic of the numerical model configuration. The bottom topography in the cross-channel direction is shown in the cross-channel plane at the open boundary; the topography in the along-channel direction is shown in the along-channel plane in the middle of the channel, denoted with stippled lines. The incoming barotropic tide is forced at the open boundary. The outgoing internal tide is excited above the continental slope near the inward end of the channel.

Figure 1b shows two rays, computed by the above ray theory. It confirms the existence of these two types of rays. One ray approaches a wave attractor at a finite distance ($x \approx -2$) from its generation point at the slope, at $x = 0$. Its shape in the cross-channel plane is identical to the one reached in Fig. 1a. This ray represents the most common type of behavior, although the trapping distance may vary depending on launch angle and position. The second ray, which is less common, straddles the critical line (near $y = 0.53$) and represents a type of edge wave. The extent to which rotation modifies the previous results will be addressed numerically.

## 3. Experimental setup

The numerical simulations were performed with the Miami Isopycnic Coordinate Ocean Model, version 2.7 (MICOM 2.7), which is an extended version of the ocean general circulation model described by Bleck and Smith (1990). Apart from the different boundary conditions and geometry, the model is similar to the one used in Drijfhout (2003) and Drijfhout et al. (2003). The present configuration consists of a channel with an open boundary at one, oceanward side and a continental slope at the opposite side. The length $L_x$ is 1200 km. The horizontal resolution is 3.75 km and there are 43 layers of 100-m depth, so that total depth $D = 4300$ m. The width of the domain $2L_y$ is 191.25 km. Figure 2 illustrates this model configuration. In this study, $X$, $Y$, and $Z$ denote dimensional Cartesian coordinates whose origin is situated at the lower boundary, at the entrance of the channel on the left. Height $Z$ is measured above the deepest point of the channel. Note that these coordinates differ from the dimensionless coordinates used in Fig. 1 that are given by $x = (X - L_x)/L_y$ and $y = (Y - L_y)/L_y$, while the vertical coordinate $z = \tau Z/D$ is stretched. In that case, coordinates have their origin at the surface on the right, in the middle of the channel, and the characteristics have an inclination of 45° with respect to the horizontal plane.

The channel is chosen to be relatively long in order to give the internal waves the chance to respond to the particular cross-channel shape of the bottom, that is either flat at a depth $D$, or parabolic. The minimum depth has been set to 50 m. The continental slope has a width of 120 km. The slope follows a sinusoidal profile, but the depth is constrained to a minimum value of 50 m. Following Bleck and Boudra (1981), the model uses a harmonic lateral diffusion, quadratic bottom stress, and a harmonic, partly deformation-dependent lateral friction:

$$\nu = \max\left\{\nu_0, \nu_u\left[\left(\frac{\partial u}{\partial x} - \frac{\partial v}{\partial y}\right)^2 + \left(\frac{\partial v}{\partial x} + \frac{\partial u}{\partial y}\right)^2\right]^{1/2}\right\}. \quad (4)$$

Here $u$ and $v$ are the velocities in along- and cross-channel direction, respectively; $\nu_0$ is a minimum back-

ground viscosity; $\nu_0 = 0.01\ \mathrm{m\ s^{-1}} \times \Delta x$, with $\Delta x$ being the grid size; and $\nu_u$ is the amplitude of the deformation-dependent part of the viscosity, with $\nu_u = 0.2(\Delta x)^2$. At the slope, lateral friction is enhanced whenever the depth is less than 800 m, where it is taken proportional to the inverse of the model depth times 800 m. This mimics enhanced dissipation in shallow seas. No wind and buoyancy forcing are applied and the diapycnal mixing is set to zero.

The flow is forced at the open boundary by a barotropic, semidiurnal tide with a typical period $T = 2\pi/\omega$ of 12 h. We have experimented with prescribing either the barotropic pressure (sea surface height) or the barotropic velocity in the along-channel direction. In both cases no profile in the cross-channel direction was assumed. It turned out that prescribing the along-channel barotropic velocity slightly reduced the partial reflection of barotropic and internal tides that is inevitable at the open boundary. In all experiments the amplitude of the tidal velocity was set unrealistically small to $10^{-3}$ m s$^{-1}$, to ensure that the model remains in the linear regime. This was motivated to facilitate comparison with (linear) theory. Consequently, all results are qualitative.

To prevent shocks, the along-channel barotropic flow was relaxed to the open boundary value with a quadratic profile, decreasing from 1 to 0 over 13 model points:

$$U_i = \alpha_i U_B + (1 - \alpha_i)\hat{U}_i, \quad i = 1, 2, \ldots, 13, \qquad (5)$$

where $U_B$ is the value at the open boundary, $\hat{U}_i$ is the unrelaxed value at grid point $i$, and

$$\alpha_i = \left(\frac{13 - i - 1}{13}\right)^2 \qquad (6)$$

(see, e.g., Holloway 1996). This relaxation zone also acts as a sponge layer for the baroclinic flow. In a similar way the baroclinic velocities were relaxed to 0 over the same 13 grid points, that is a patch of 48.75-km width. Ideally one would prefer to use a radiation condition for the internal wave field at the open boundary. Various formulations have been tested (Orlanski 1976; Raymond and Kuo 1984; Flather 1988), each of them worked reasonably well in case of a flat bottom and no rotation; none of them worked in case of rotation and a quadratic bottom slope in the cross-channel direction. So, we relied on a sponge layer for the baroclinic velocities at the open boundary. Although most of the outward-propagating wave field is absorbed, a sponge layer is always partially reflecting. To minimize reflection, an along-channel phase velocity for the internal wave field was estimated in the sponge layer by calculating the phase velocity for the baroclinic pressure field according to Orlanski (1976). When wave propagation was oceanward, the interface displacement $h$, or pressure $p$ was left unaffected. The interface displacement was calculated by vertically integrating the (anomalous) layer thickness of each isopycnal layer. The layer thickness itself is a prognostic variable obeying a continuity equation. When inward propagation was found, the phase velocity of the neighboring inward grid point was used to calculate a new value for $h$ from the Orlanski (1976) radiation condition. Although this procedure did not eliminate all wave reflection in the sponge layer (interference of an outward-propagating and reflected inward-propagating wave may still yield net outward propagation in which case $h$ is left unaffected), it helped to improve the solution. Extending this procedure to a wider zone than the sponge layer did not have any effect.

Four experiments are discussed in this paper. In two experiments the earth's rotation is neglected and the Coriolis frequency $f = 0$. In the other two experiments we use an $f$ plane with $f = 10^{-4}$ s$^{-1}$. Both cases are run with two channel configurations: in one case the channel has a flat bottom at 4300-m depth and vertical walls in the cross-channel direction; in the other case the channel has a parabolic cross-channel bottom profile with a maximum depth of 4300 m and sloping sidewalls. In the case of no rotation the buoyancy frequency was chosen as $N = 3.05 \times 10^{-3}$ s$^{-1}$, in the case of rotation $N = 2.2 \times 10^{-3}$ s$^{-1}$. These values were motivated to keep the lumped parameter $\tau$ to be equal for all experiments. For channels with a parabolic bottom profile and $0.87 < \tau < 1.0$ the internal wave is expected to be trapped onto a simple-shaped symmetric attractor (e.g., the one reached in Fig. 1a). In all four experiments, $\tau = 0.94$ right in the middle of the trapping regime for the sloping-bottom runs. For the flat-bottom runs no focusing is expected and therefore no trapping.

## 4. Results

### a. Trapping

A barotropic tide forces stratified water to oscillate over topography, which generates long internal waves or internal tides. Baines (1982) suggested that a critical parameter that determines the strength of the internal tides that are generated was given by: $r = \alpha/c$, where $\alpha$ is the local bottom slope and $c$ again denotes the slope of the internal wave characteristics, Eq. (2), which is fixed for any given frequency. Note the similarity with our lumped parameter $\tau$. Baines argues that generation is strongest when $r$ is approximately 1 (i.e., when the bathymetry has a critical slope). Therefore, unless a

supercritical region of the slope exists, the generation of internal tides is likely to be weak (Holloway and Merrifield 1999). The model used here features a sinusoidal slope near the inward boundary. The slope is steepest at $X = 1140$ km, where $r = 1.11$. The slope is supercritical between $X = 1131$ km and $X = 1149$ km. The points $X = 1131$ km and $X = 1149$ km define the concave and convex critical points, respectively, where the slope $r = 1$. Figure 3a illustrates the internal tide generation above the continental slope in the flat-bottom run without rotation. Shown is the magnitude $A$ in centimeters of the complex harmonic amplitude (that also contains phase $\phi$), which is obtained by a projection of the model field after 15 days of runtime onto the forcing frequency (harmonic analysis):

$$A(x, y, z) \exp[i\phi(x, y, z)] = \int_{T_{15}}^{T_{16}} h(x, y, z, t) \exp(i\omega t)\, dt. \tag{7}$$

Here $T_n$ denotes the start of day $n$ (i.e., after $2n$ tidal periods). As the forcing amplitude is very small, the flow is linear and the response to the forcing is almost completely contained in the forcing frequency $\omega$. In the present experiment the harmonic analysis was performed with 16 output fields that were saved between days 15 and 16, sampling twice the tidal period with 8 fields during each tidal cycle.

In Fig. 3a, the internal tide manifests itself as a beam that propagates obliquely, both in the horizontal as well as the vertical direction as observed at sea (Pingree and New 1991). The wave progresses outward, opposite to the direction of the incoming barotropic tide. It gradually diminishes due to dissipation by friction and diffusion. At the open boundary there are no signs that the signal is degraded by spurious reflections. The internal tide features five reflections at the sea surface and six at the bottom. The wavelength, determined by characteristic slope $c$ [Eq. (2)], and the depth of the fluid (4300 m), is about 200 km.

About halfway the slope, a weaker, initially upward-moving beam can be seen, which reflects 6 times at the surface and 5 times at the bottom. New (1988) predicted that three beams would emanate from the convex, upper critical point, which, in that model, occurred at the shelf break where the linear slope was connected to the flat shelf. One beam radiated downward into the deep sea, one upward onto the shelf. But later it was argued that the third, initially upward and oceanward beam was elusive (e.g., Gerkema et al. 2004; Azevedo et al. 2006) because the induced fluid motion would not satisfy the bottom boundary conditions. However, here we see that a third beam does occur, emanating from the concave, lower critical point at $X = 1131$ km (indicated by an arrow in Fig. 3a). This presumably results from convergence of bottom boundary layer transport. For this critical point, the only possible motion is upward, away from the bottom slope and as a result the third beam emerges.

The 2D, inviscid stationary wave theory predicts that when the cross-channel bottom profile is parabolic, a simple-shaped wave attractor of the internal tide will occur for the parameters used here (Maas and Lam 1995). Strictly speaking, the theory applies to 2D flows and holds only for rays propagating in the cross-channel direction. However, when the sloping sidewalls have enough curvature (i.e., contain both a supercritical as well as subcritical part), the rays will refract toward the cross-channel direction in a 3D configuration. The question now is whether refraction will cause wave motion to become sufficiently oriented in the cross-channel plane to make trapping possible in 3D. The answer is given by Fig. 3b. Trapping indeed occurs and the main beam can no longer be distinguished for $X <$ 800 km.

Figure 4 shows the amplitude at a cross-channel section at $X = 990$ km to illustrate that trapping occurs in the cross-channel plane. The attractor, as predicted from 2D theory, is indicated by black lines and the amplitude of interface displacement clearly displays maxima along the attractor. We also see from Fig. 4 that the attractor is associated with small-scale gradients in the wave field, a consequence of the repeated focusing. Even higher amplitudes can be found in the upper-left and -right corners, outside the attractor domain. This is because the barotropic tide will attain a 3D structure. At first sight this may seem surprising, as in the present case the channel is nonrotating and the barotropic currents might be expected to be oriented strictly in along-channel direction. However, the bottom slope has a cross-channel component, so that near the slope, at the end of the channel, the reflected barotropic tide also acquires a cross-channel component such that part of its motion is directed in cross-channel direction. As a result, there is a continuous conversion from the barotropic to the baroclinic tide all along the cross-channel slope, with a maximum conversion near the along-channel boundaries where the slope is steepest.

To make comparison possible with Fig. 3a, Figs. 3b and 4 make use of the harmonic analysis of the data of days 15–16. All other figures for this experiment show results from the harmonic analysis of data of days 3–4. Because part of the outgoing internal waves reflect at the sponge layer near the open boundary, interference of the outward-propagating waves with reflected, inward-propagating waves occurs as time proceeds. As a

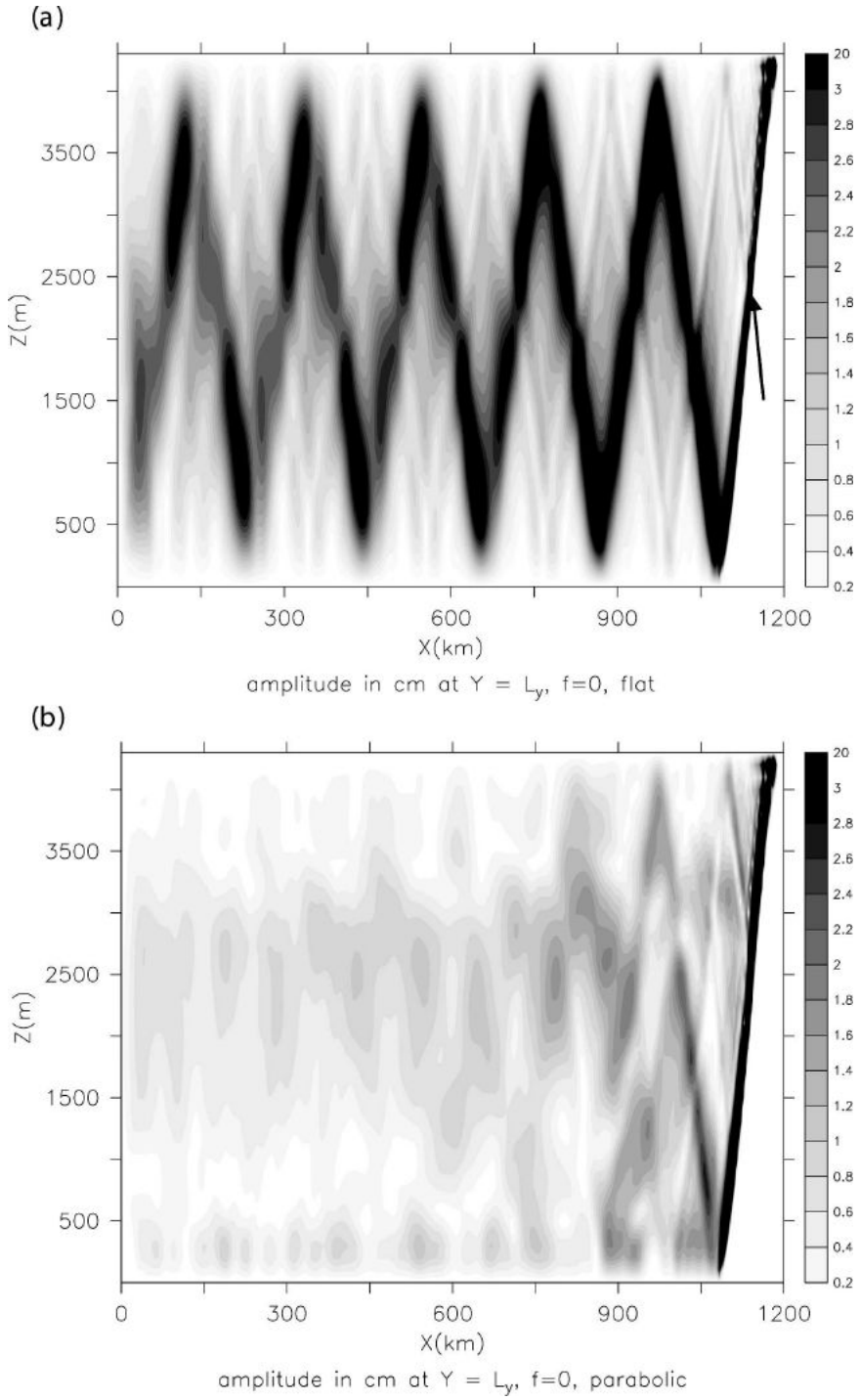


FIG. 3. (a) An along-channel cross section in the middle of the channel of the harmonic amplitude of interface displacement in centimeters for the flat-bottom run without rotation, obtained at days 15–16. This figure shows unimpeded oceanward propagation of the internal tide. Over the concave critical point on the slope at $X = 1131$ km (indicated by an arrow) an upward, oceanward beam is generated. (b) Harmonic amplitude of interface displacement for the sloping-bottom run without rotation. This figure shows trapping of the internal tide due to geometric focusing.

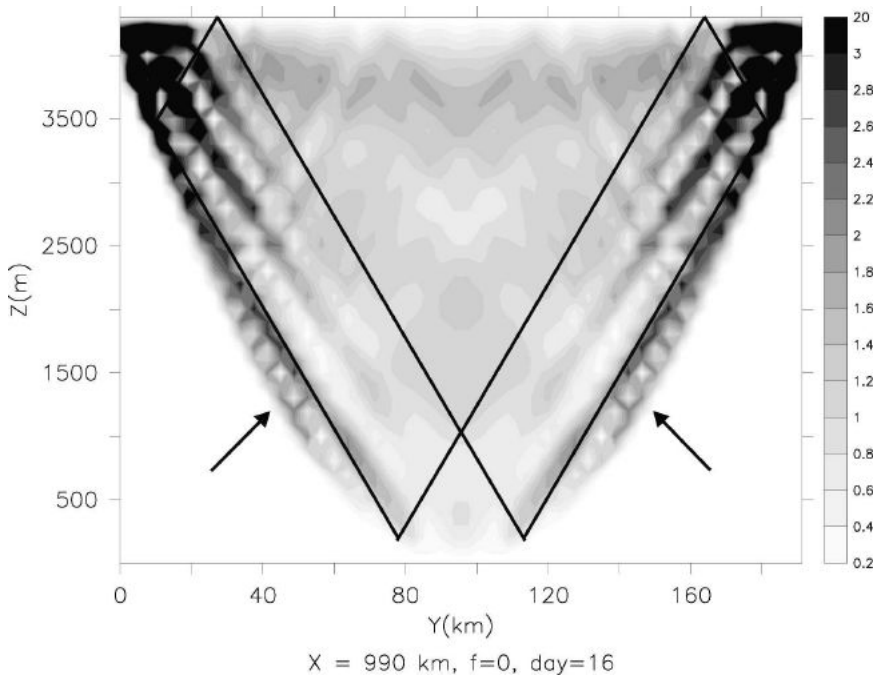


FIG. 4. A cross-channel section at $X = 990$ km of the harmonic amplitude of interface displacement in centimeters for the sloping-bottom run without rotation. Superimposed is the predicted 2D attractor. This figure shows that energy is maximized on the attractor. Arrows indicate the locations where the cross-channel slope is critical and where along-channel corridors exist along which waves may leak away.

result, in each run a compromise in runtime had to be found, allowing the wave field to develop in time, but at the same time minimizing reflection from the open boundary sponge layer. In the sloping-bottom runs the runtime was 4 and 5 days for the runs without and with rotation, respectively; in the flat-bottom runs the runtimes were longer, allowing the full wave field and higher baroclinic modes to reach the open boundary (i.e., 12 days for the run with rotation and 16 days for the run without rotation).

Inspection reveals strong phase gradients in the lower half of that same cross section, perpendicular to the cross-channel slope (Fig. 5a). The total phase angle $\omega t - \phi$ is constant with progressing time when $\phi$ increases. From the phase gradients we infer that phase propagate obliquely upward and inward; for height $Z <$ 2000 m the phase gradients are almost perpendicular to the slope, pointing to the center of the channel, which implies that energy moves downward along isophase lines; from $Z > 2000$ m upward, in the middle of the channel, phase lines are aligned along the cross-channel slope and propagate toward the bottom so that energy propagates upward. Figure 5b shows an along-channel cross section of the phase at $Y = 56.25$ km, where the phase gradient near the bottom is large in the cross-channel plane at $X = 990$ km, as shown in Fig. 5a. Figure 5b shows that, except near the continental slope, phase (and also energy) progresses oceanward, illustrated by the nearly vertical alignment of phase lines. Along the continental slope, upward energy propagation, implied by the phase field at $X = 1065$ km (Fig. 6), is in the opposite direction to the energy propagation at $X = 990$ km. (Note that the phase gradient perpendicular to the sloping bottom in the lower half of the domain is opposite to the gradient shown in Fig. 5a.) This upward energy propagation occurs just after the first bottom reflection of the downward-propagating beam that was generated at the continental slope.

### b. The edge wave

There exist two along-channel corridors of limited extent in the $Y$ direction and centered around the concave critical lines, along which waves may leak away perpendicular to the previously considered cross sections. One such corridor can be associated with the rays of Fig. 1b that cluster around the critical lines in an endless succession of focusing and defocusing reflections (Maas 2005). These rays represent an internal edge wave. Theoretically, the critical line is at height $Z = 1300$ m. The edge wave manifests itself at somewhat shallower depth, around height $Z = 2000$ m (see Fig. 7a). Figure 7b clearly shows how energy leaks away

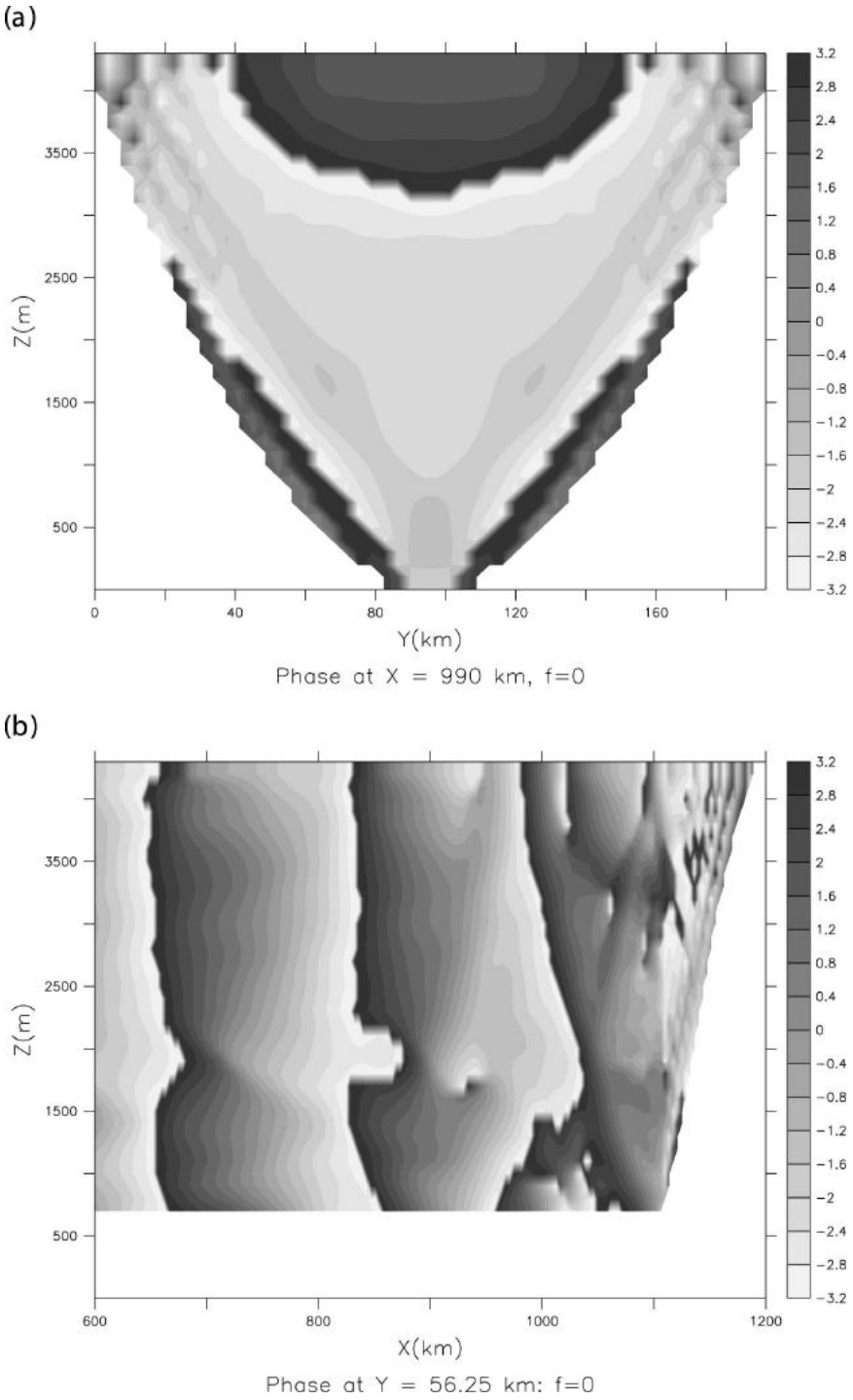


FIG. 5. (a) The phase field associated with Fig. 4, showing upslope phase and hence downslope energy propagation in the cross-channel plane. Apart from Figs. 3b and 4, all figures for this experiment use the harmonic analysis on the fourth day of the integration. (b) An along-channel cross section of the phase at $Y = 56.25$ km, showing oceanward phase and energy propagation in the cross-channel plane.

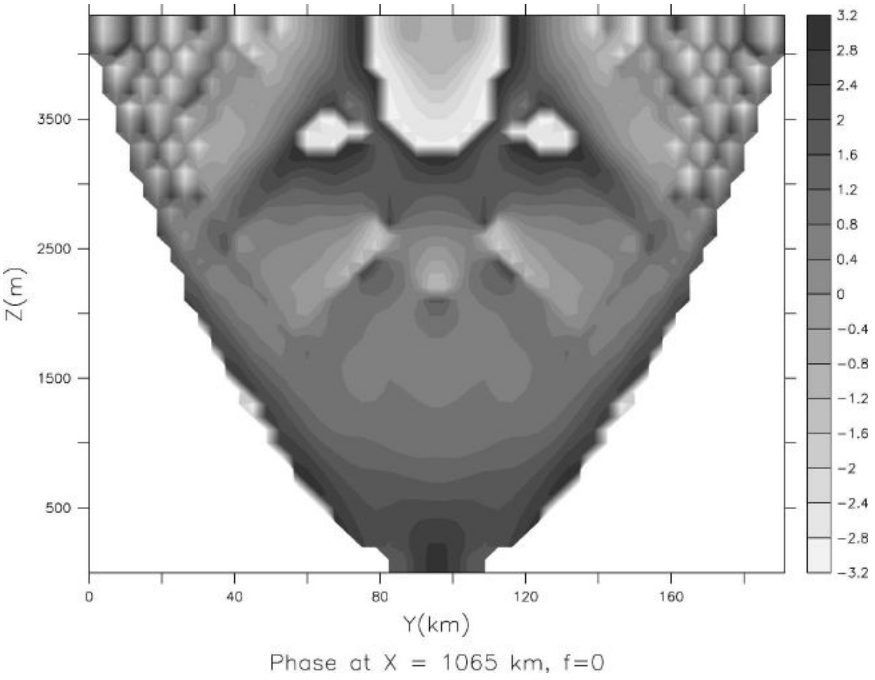


FIG. 6. Meridional cross section of the phase field at $X = 1065$ km, showing upward energy propagation, in contrast with Fig. 5a.

along the boundaries, while in the middle of the channel the energy remains trapped near the continental slope (cf. Figs. 3b and 7b).

An even more dramatic illustration of the edge wave is given by Fig. 8. This figure shows horizontal cross sections of the wave amplitude at height $Z = 2300$ m, comparing the runs with a flat and a sloping bottom. The flat-bottom case shows a plane internal gravity wave that propagates oceanward and gradually loses energy by friction. In the inward half of the channel, the sloping-bottom case shows trapping of the internal gravity "wave" (as it no longer clearly propagates it has lost part of its wave properties) in the middle of the domain, and leakage along the boundaries by an edge wave. The edge wave has a double structure, reminiscent of the two nearly vertical branches of the edge wave ray pattern in Fig. 1b.

### c. *The effects of rotation*

The main effect of rotation is breaking of the cross-channel symmetry that is associated with the runs without rotation. In the case of a flat bottom, the plane internal gravity wave is replaced by internal Poincaré modes that are quantized in the vertical and cross-channel directions, determined by wavenumbers $n$ and $m$, respectively. These modes move outward unless $\tau > 2n/m$, when they are trapped to the slope (LeBlond and Mysak 1978, their section 28). In our domain, the $m = n = 1$ mode seems to dominate, having a node at 65% of the channel width (see Fig. 9). Moving along the boundary to its right we also find an internal Kelvin wave with maximum amplitude at the wall decaying exponentially with distance from that wall. A horizontal cross section (Fig. 10a) clearly demonstrates that the Poincaré and right-bound Kelvin waves have different along-channel wavelengths. A cross section of the phase field (Fig. 10b) underscores that the Poincaré and Kelvin waves propagate independently, with a complex superposition near the nodal point, at $Y \approx 145$ km.

When sloping sidewalls are included the symmetric signature of the trapped internal gravity wave, characteristic for the rotation-off solution (Fig. 3b), is now, with rotation on, replaced by the asymmetric signature of a combination of trapped Poincaré and Kelvin waves (Fig. 11). At $X = 945$ km (Fig. 12), the phase field only shows the oblique upward movement, perpendicular to the slope, and along-slope, downward movement of energy that was characteristic for the attractor in the no-rotation case (Fig. 5), near the wall where the right-bound Kelvin wave resides. The trapped Poincaré wave, especially visible at the opposite wall, shows hardly any phase propagation, and is completely arrested.

Comparing horizontal cross sections of the cases with and without rotation reveals some remarkable differences. In both cases trapping of energy in the middle of

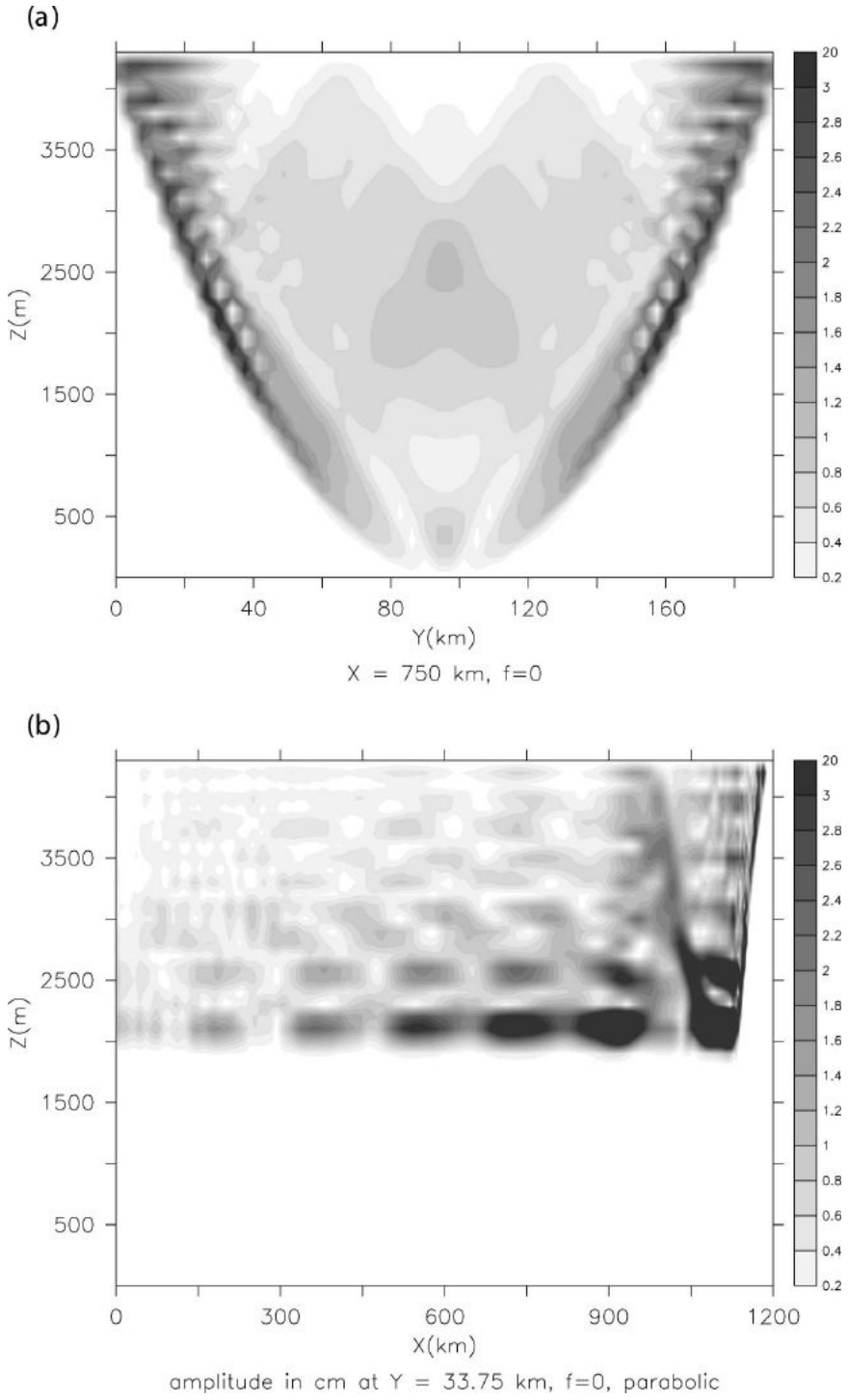


FIG. 7. (a) Meridional cross section of the harmonic amplitude of the interface displacement at $X = 750$ km, and (b) zonal cross section of the same field at $Y = 33.75$ km showing the edge wave for the sloping-bottom run without rotation.

the channel occurs close to the continental slope at the right (Fig. 13). High amplitudes of interface displacement at $Y = 95$ km can be seen between 800 km $< X <$ 1100 km. Without rotation, energy propagates from the walls into the interior, visible by the oblique lines of maximum amplitude that emanate from the walls with approximate 150-km intervals. For example, one such a line can be traced in the top panel of Fig. 13, from ($X =$

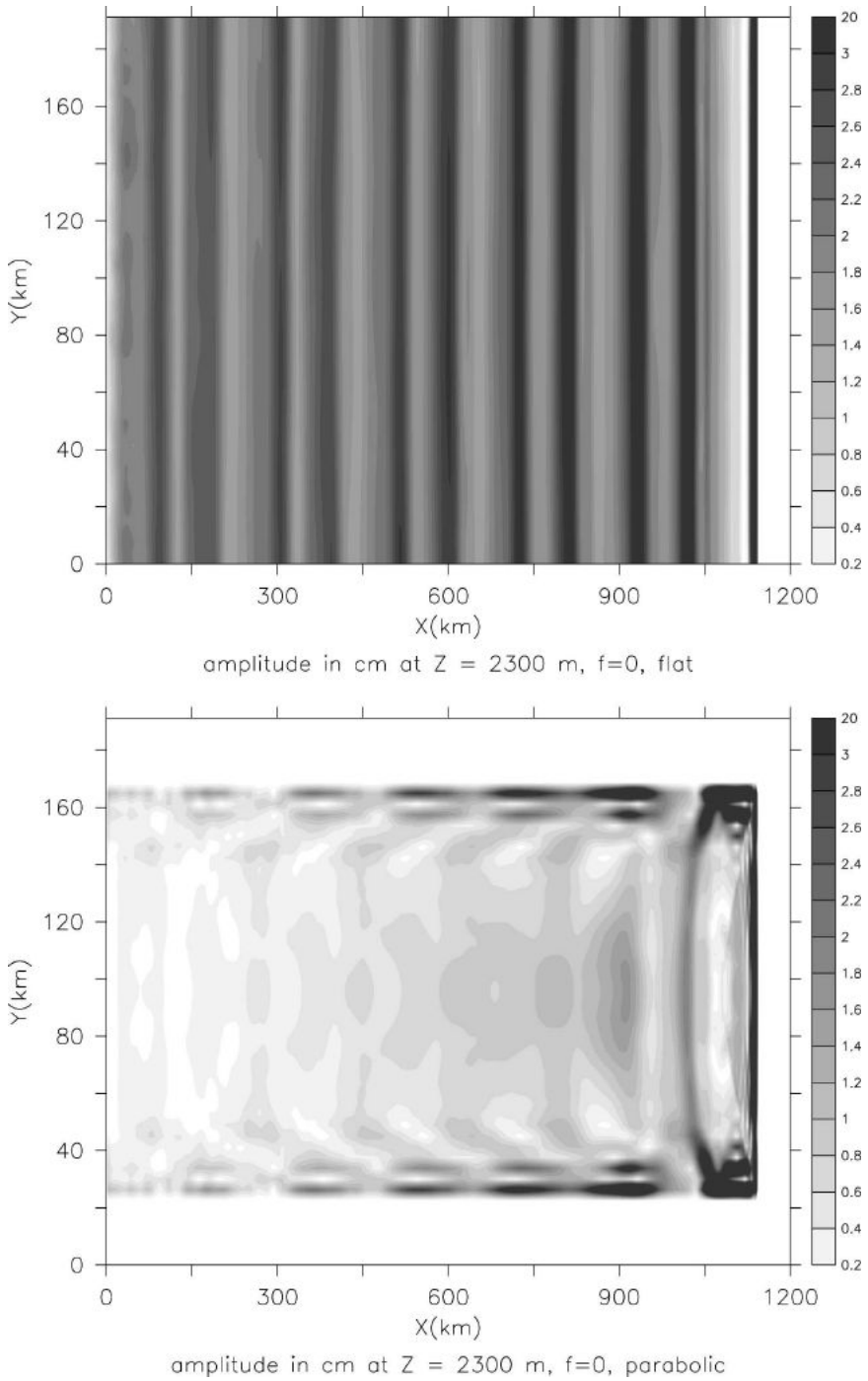


FIG. 8. Two horizontal cross sections of the amplitude of interface displacement at height $Z = 2300$ m when rotation is off. (top) The flat-bottom case and (bottom) the sloping-bottom case. This figure shows geometrical trapping and the outward-propagating edge waves.

950, $Y = 45$) to ($X = 700$, $Y = 75$). When rotation is on, this leakage of energy from the sidewalls into the interior is absent, see the bottom panel of Fig. 13. As a result, the along-channel penetration of edge waves is increased, while in the middle of the channel the penetration of the energy is decreased. This increased penetration of the edge waves can be inferred from the higher amplitudes at $Y = 45$ and $Y = 145$ km for $X <$ 400 km in the bottom panel of Fig. 13. Also, it appears that the arrested Poincaré wave is more perfectly

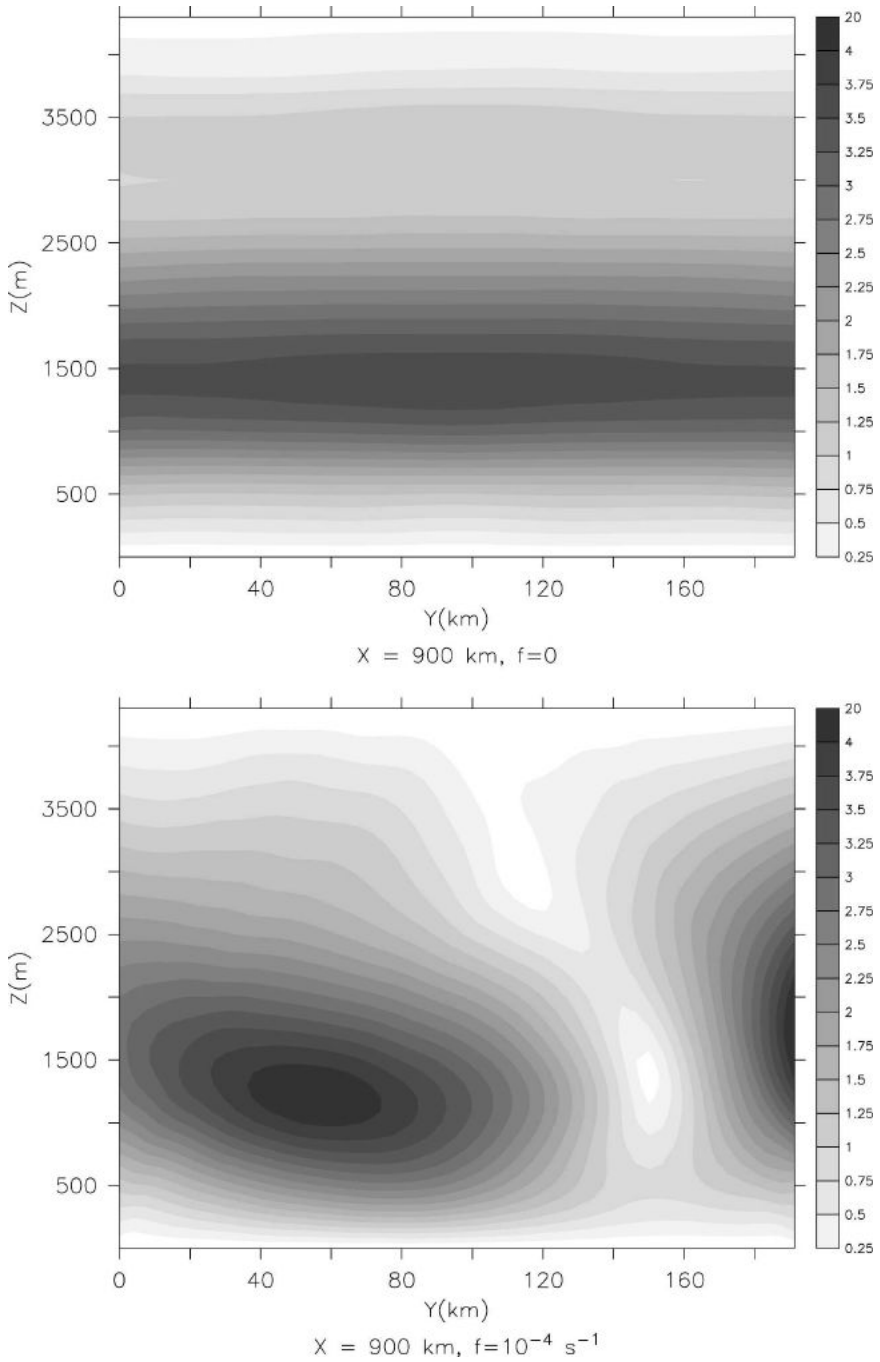


FIG. 9. Meridional cross sections of the amplitude of interface displacement at $X = 900$ km for the flat-bottom geometry. (top) The plane internal gravity wave when rotation is off and (bottom) the combination of a Poincaré and a right-bound Kelvin wave when rotation is on.

trapped than the right-bound Kelvin wave or the plane wave in the no-rotation case. Apparently, the absence of strong phase gradients (see Fig. 12) is associated with a more complete stagnation of the outgoing energy flux than in case of a phase gradient signature that is associated with the 2D attractor in the cross-channel plane.

Figure 14 presents an illustration of the evolution of the combination of internal waves trapped in the middle and leaky edge waves at the boundary. Initially, near the continental slope the trapped Poincaré waves and left-bound edge wave dominate the signal. Farther downstream, the right-bound edge wave becomes

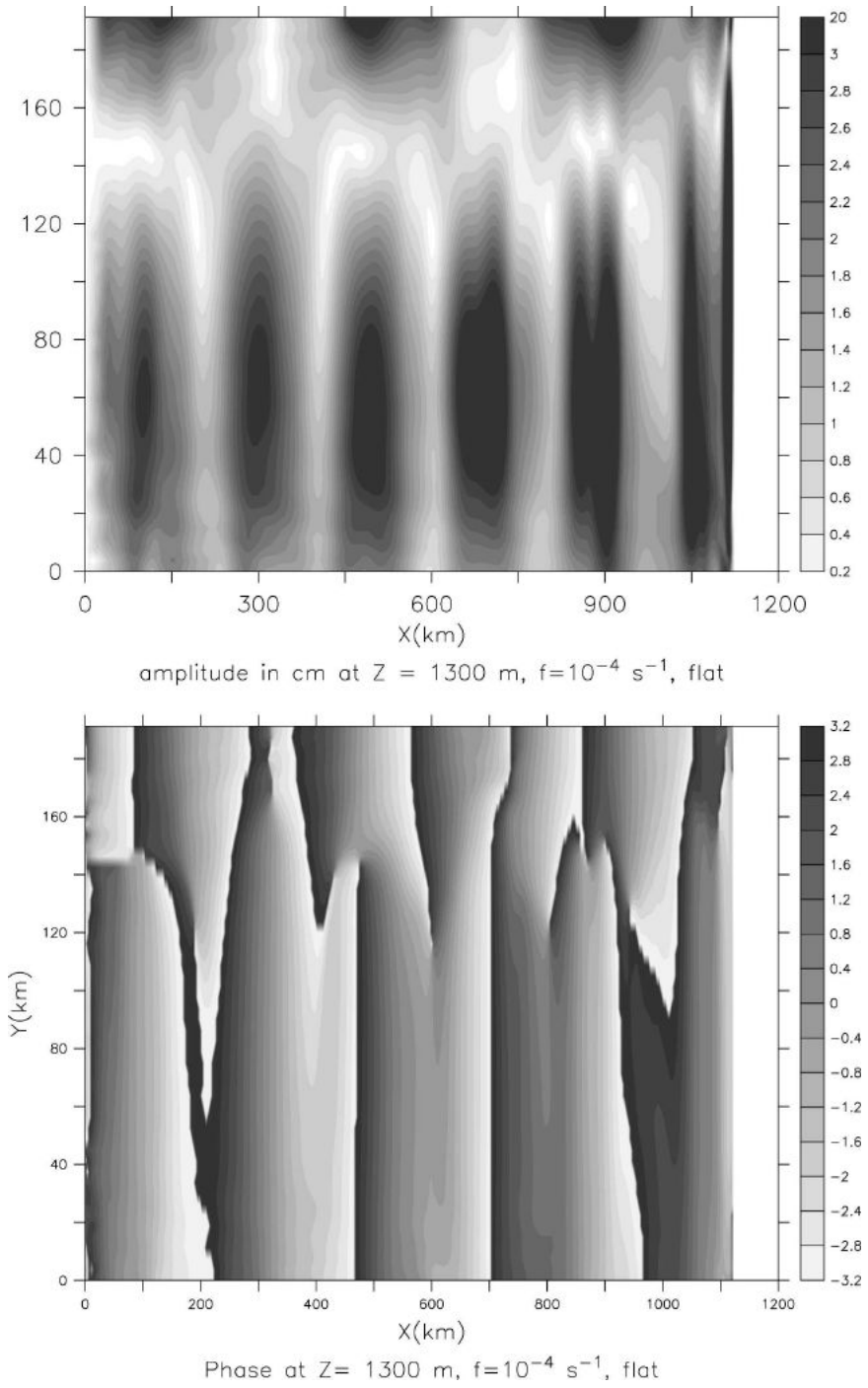


FIG. 10. (top) A horizontal cross section of the amplitude of interface displacement at height $Z = 1300$ m for the flat-bottom run when rotation is on. This figure shows that the Poincaré (bottom part of each panel) and Kelvin wave (top part) have different wavelengths. (bottom) The phase field for the same run, showing that the Poincaré and Kelvin waves propagate independently.

stronger. This asymmetry is further illustrated by the along-channel cross sections of Fig. 15. In the middle of the channel trapping is even stronger than in the case without rotation (cf. Figs. 3b and 15a), due to the lack of energy leakage from the boundaries to the middle when rotation is on. The left-bound edge wave (Fig. 15b) shows more signs of oblique, upward propagation than its right-bound counterpart (Fig. 15c). As a result,

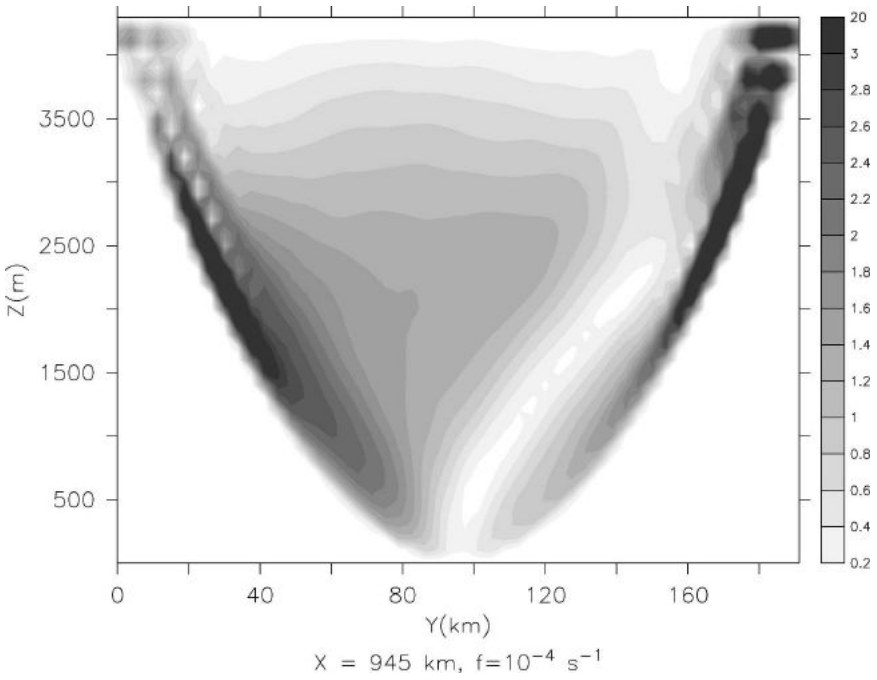


FIG. 11. A cross-channel section of the amplitude of interface displacement at $X = 945$ km for the sloping-bottom run with rotation on. The "trapped right-bound Kelvin wave" shows marks of the 2D wave attractor, while the "trapped Poincaré wave" deviates stronger from the case without rotation (cf. Fig. 4).

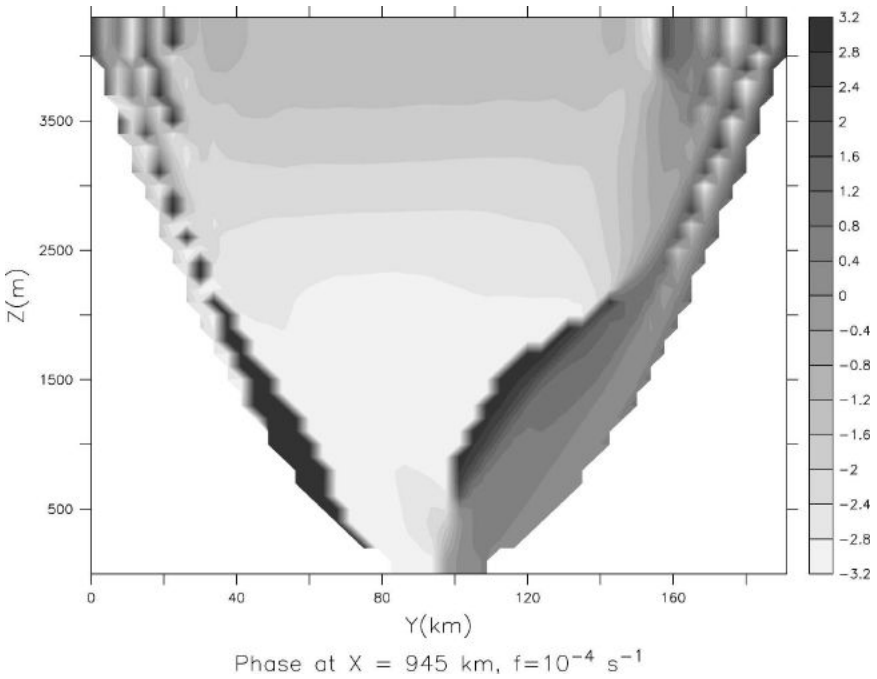


FIG. 12. The phase field belonging to Fig. 11. Downslope energy propagation is associated with the trapped right-bound Kelvin wave, with phase gradients perpendicular to the slope in the lower right, similar to the phase gradients displayed in Fig. 5a. At the opposite slope the phase gradients are weaker.

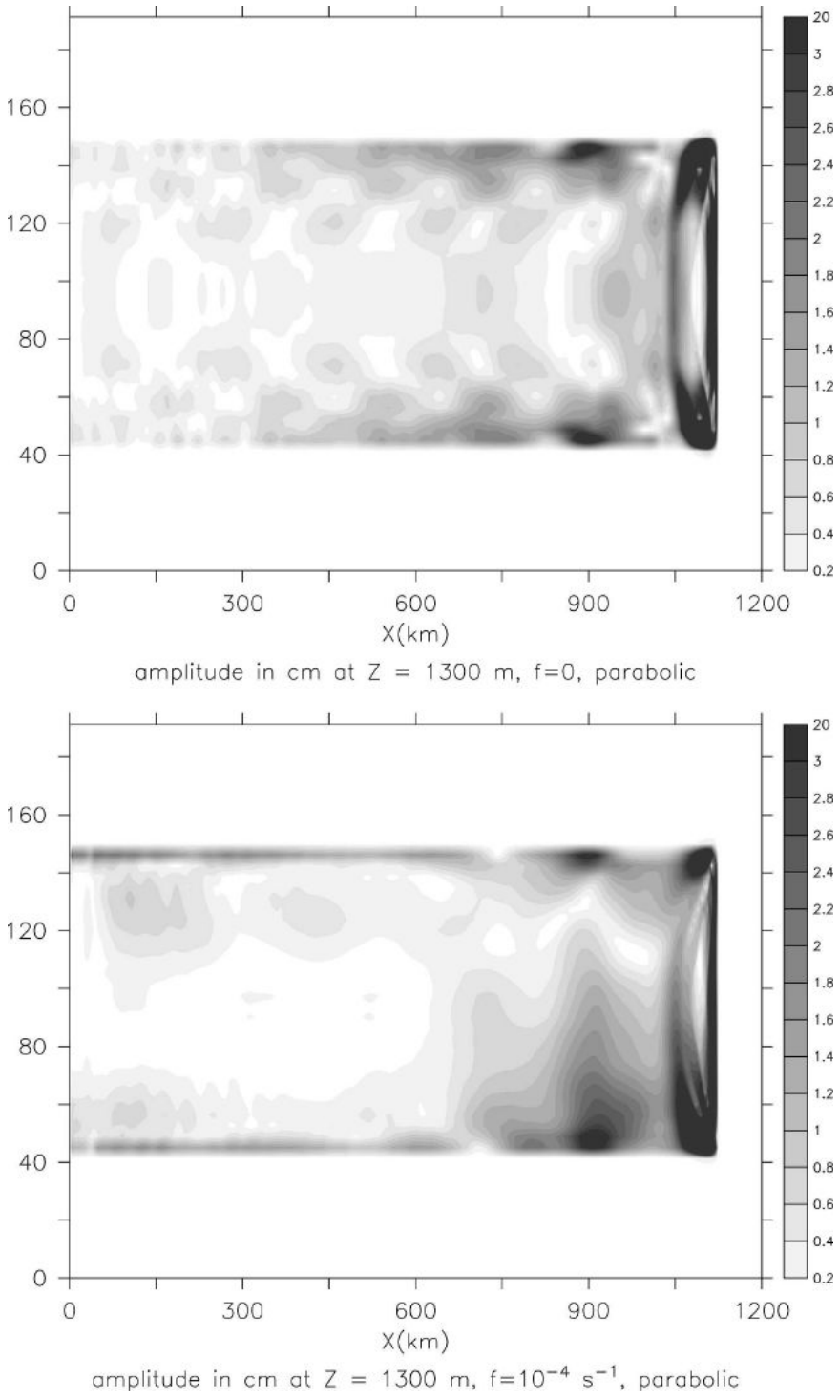


FIG. 13. Two horizontal cross sections of the amplitude of interface displacement at height $Z = 1300$ m for the sloping-bottom geometry. (top) The case without rotation and (bottom) the case with rotation on. This figure shows increased along-slope trapping of the edge waves when rotation is included. Without rotation, energy leaks from the sidewalls to the middle of the channel.

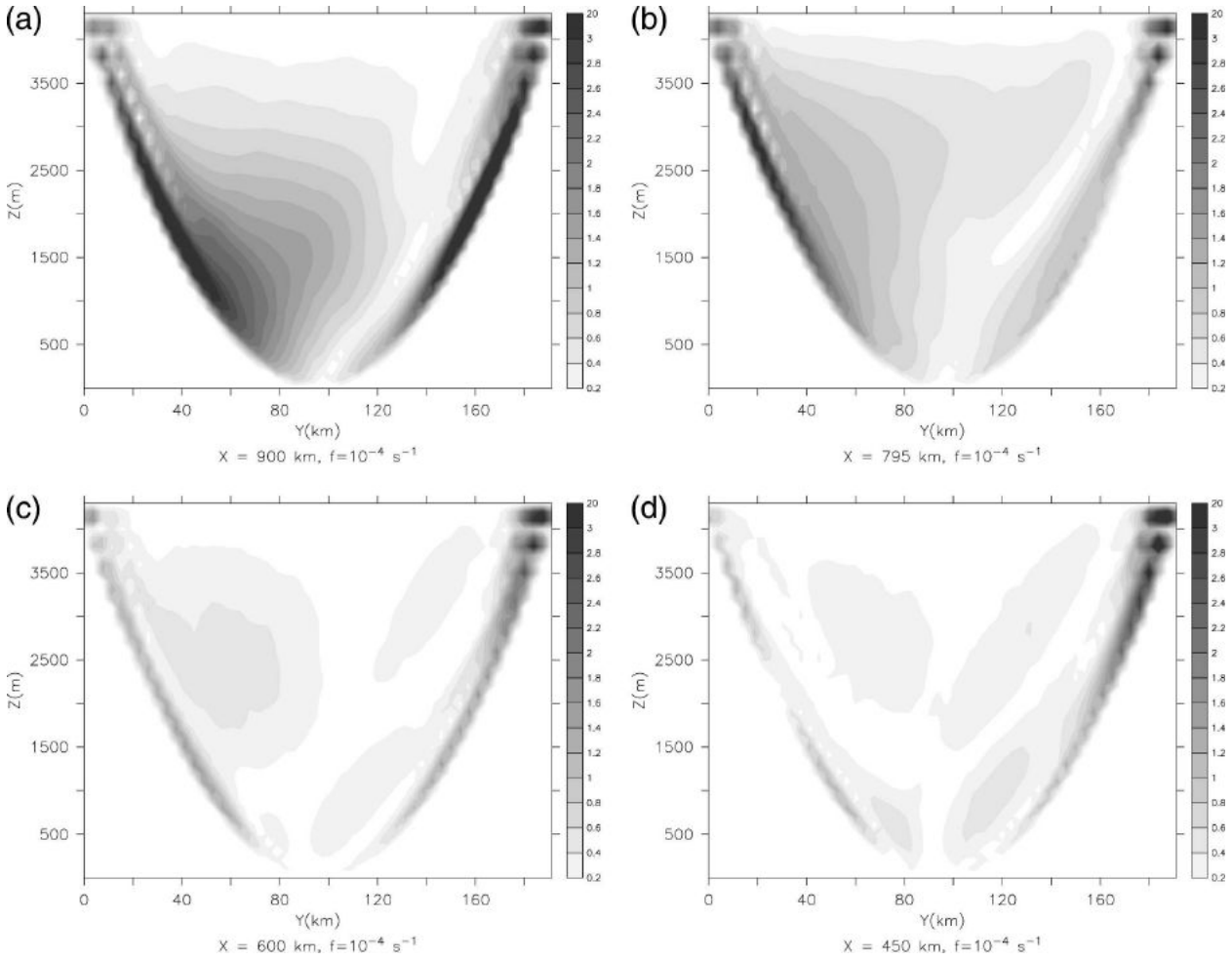


FIG. 14. Four cross-channel sections of the amplitude of interface displacement for the sloping-bottom run with rotation on. The cross sections are taken at $X = 900$ km, $X = 795$ km, $X = 600$ km, and $X = 450$ km. This figure illustrates that the along-channel propagation of the right-bound edge wave becomes more dominant when the distance from the continental slope increases.

the right-bound edge wave has a larger along-channel penetration and shows more signs of reflection at the sponge layer, as can be inferred in Fig. 15c from the higher amplitudes near $Z = 2000$ for $X < 600$ km.

A second reason why the right-bound edge wave has a larger along-channel penetration is suggested by Fig. 16. At the top of the slope, along the boundary, the reflected barotropic tide acts as a secondary source for the internal tide. There is an energy maximum at height $Z = 4200$ m that propagates downward along the slope. The energy maximum manifests itself by the high amplitudes at $180 < Y < 190$ km for $X < 600$ km, while the edge wave itself is not present at this height, being centered around $Z = 3000$ m (see Fig. 14). When rotation is on, the reflected barotropic tide manifests itself mainly as an outgoing, right-bound Kelvin wave. Contrary to the textbook example of a Kelvin wave that travels along a vertical boundary, this reflected, barotropic Kelvin wave has an associated cross-channel motion, perpendicular to its direction of propagation (Le Cann 1990). Because of the cross-channel slope, this motion acquires a vertical component and by lifting isopycnals acts as the source for the right-bound internal edge wave. Along the opposite boundary such a secondary source for the internal tide is absent, which is illustrated by the much lower amplitudes between $0 < Y < 10$ km.

## 5. Energy transport

A summary of the previous results on geometric trapping of the internal tide can be given by comparing the depth and cross-channel integrated horizontal baroclinic energy fluxes for all four runs discussed. The energy flux $E$ is defined as the transport of energy past a point and averaged over a tidal period. We consider the

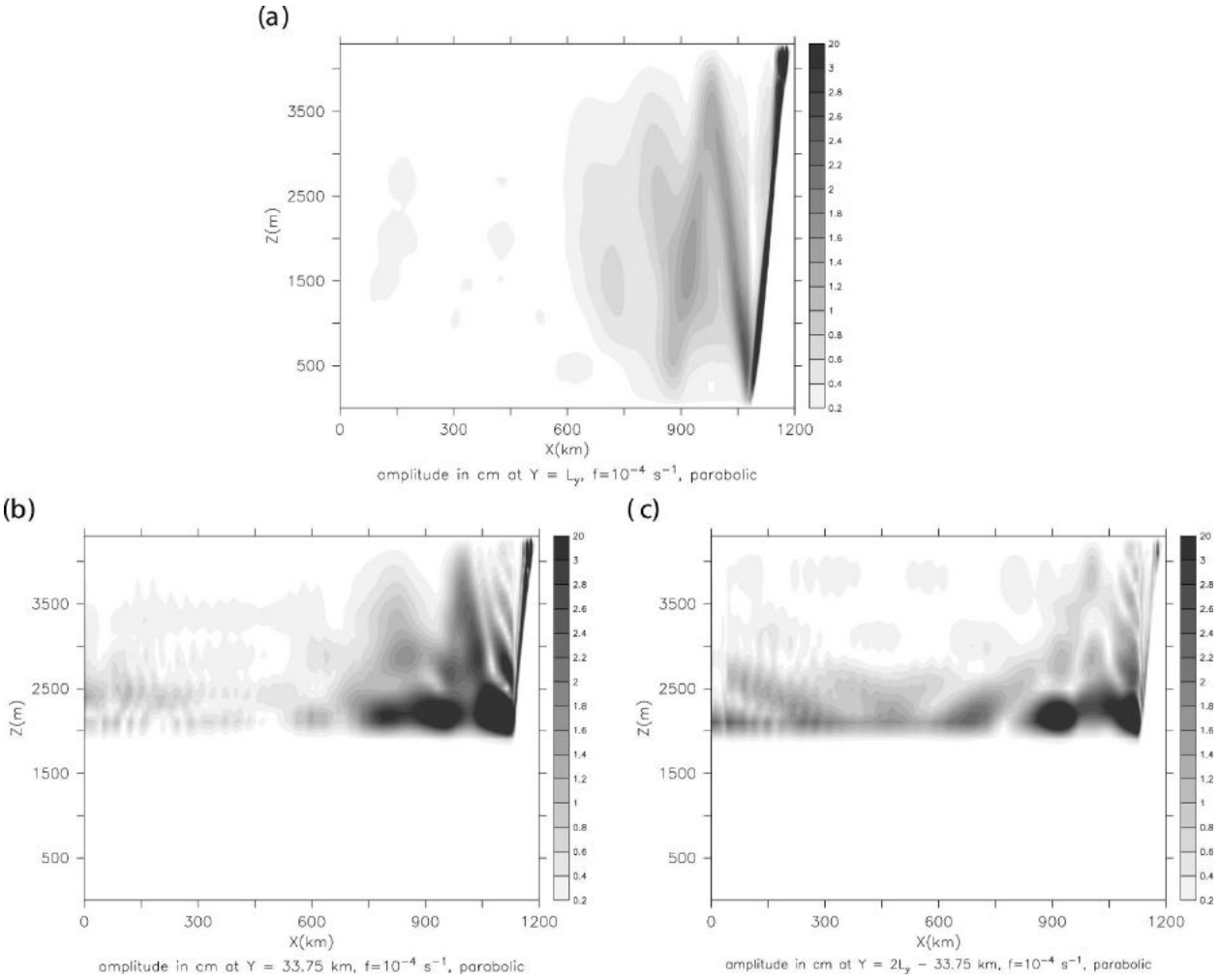


FIG. 15. Three along-channel cross sections for the same case as shown in Fig. 14. (a) In the middle of the channel, showing the "trapped Poincaré waves." (b) Near the boundary at $Y = 33.75$ km, showing the left-bound edge wave and trapped Poincaré wave. (c) Near the boundary at $Y = 2L_y - 33.75$ km, showing the right-bound edge wave and "trapped Kelvin wave." It is shown that along-channel propagation along the boundary at the right dominates over propagation along the boundary at the left.

down-channel energy transport by baroclinic motions only; thus,

$$E = \frac{1}{T}\int_0^T up\, dt, \tag{8}$$

where $T = 2\pi/\omega$ is the tidal period, $u$ is the along-channel baroclinic velocity, $p$ is the fluctuating part of the baroclinic pressure, and $t$ is time. In general it is more convenient to consider the depth-integrated energy flux $F$ through a cross-channel plane:

$$F = \frac{1}{A}\int_0^{2L_y}\int_0^D E\, dZ\, dY, \tag{9}$$

with $A = \int_0^{2L_y} D(Y)\, dY$ is the cross-channel area. In isopycnic coordinates this becomes

$$F = \frac{1}{AT}\int_0^T\int_0^{2L_y}\int_0^D uM\, dh\, dY\, dt, \tag{10}$$

where $h$ is the layer depth and $M$ is the fluctuating part of the Montgomery potential (see Bleck and Smith 1990).

Lu et al. (2001) have argued that the baroclinic energy transport includes a contribution that is associated with density and baroclinic pressure variations due to heaving by the surface tide. As a result, the baroclinic energy flux exhibits large-amplitude periodic variations in $X$ over regions where the bottom slope is independent of $X$. They proposed a method to separate surface and internal tide components in the baroclinic energy flux. Applying this procedure to the isopycnic coordi-

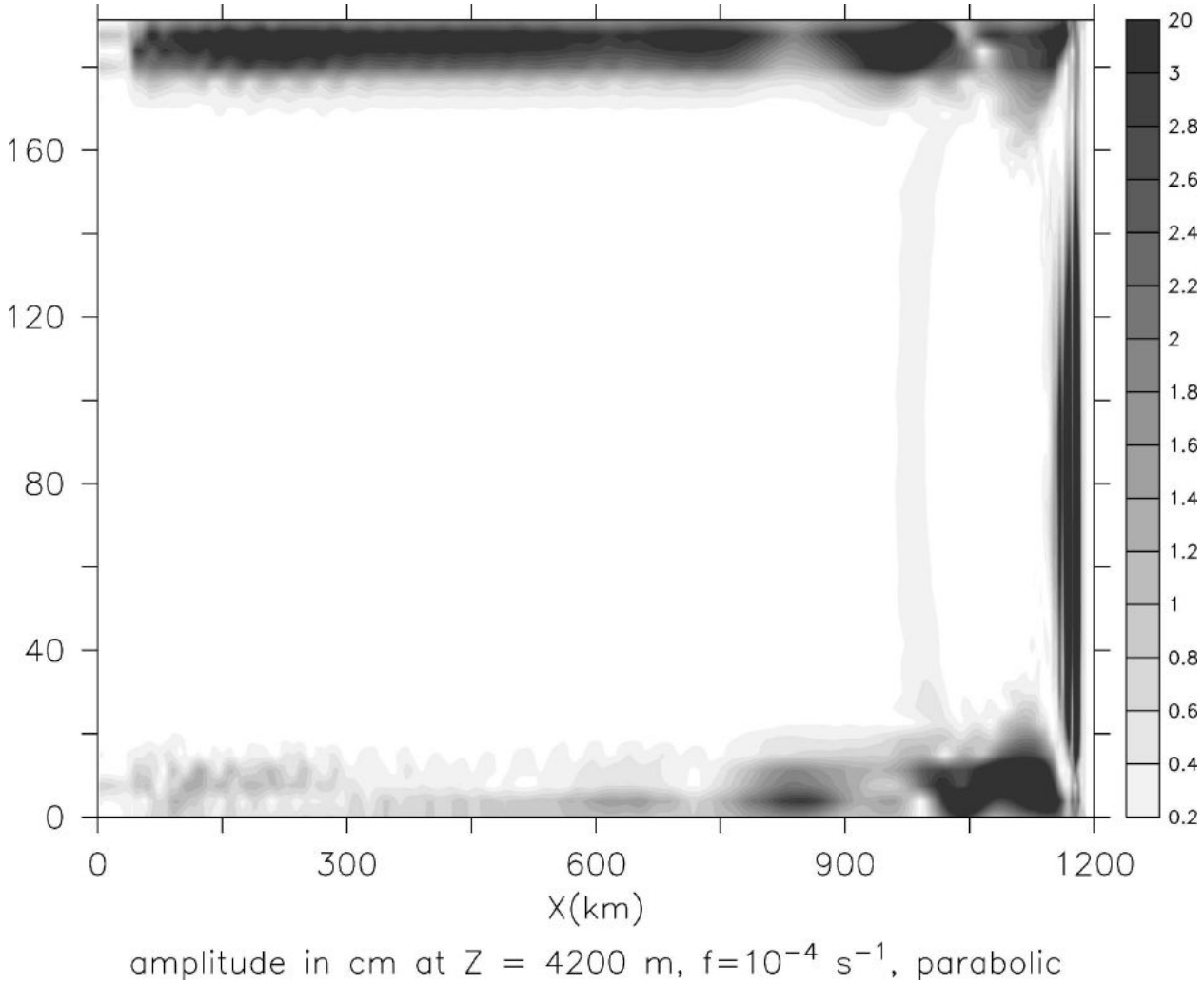


FIG. 16. A horizontal cross section of the amplitude of interface displacement at height $Z = 4200$ m for the run discussed in Fig. 15. This figure shows that the cross-channel upslope motion of the barotropic right-bound Kelvin wave acts as a secondary source for the internal tide.

nate framework implies that in Eq. (10), $M$ has to be replaced by a quantity $M^*$, where $M^*$ is defined as

$$\frac{\partial M^*}{\partial s} = p^* \frac{\partial \rho^{-1}}{\partial s}, \tag{11}$$

where $\rho$ is the density, $p^*$ is the fluctuating baroclinic pressure from which the tidally averaged pressure change due to divergence of the barotropic mass transport is subtracted, and $s$ is the vertical (isopycnal) coordinate.

The resulting energy flux will be negative over most of the region in the four experiments discussed above, implying oceanward energy transport. For comparison, we scale the energy transport in all runs with the minimum value. The result is displayed in Fig. 17. In the flat-bottom runs the decrease in energy transport is larger when rotation is on, probably because some of the Poincaré waves are trapped in the along-channel direction, contrary to the internal gravity waves in the case without rotation (LeBlond and Mysak 1978). The parabolic channel runs clearly show that the penetration scale of the energy transport away from the continental slope significantly decreases by geometric focusing due to a sloping bottom in the cross-channel direction. When rotation is on, trapping is even stronger than without rotation. While rotation apparently inhibits the constant leakage of energy from the sidewalls toward the middle of the channel that occurs in the latter case (see Fig. 13a), it still provides further rotational constraints on the down-channel propagation, in particular, by completely arresting the Poincaré wave.

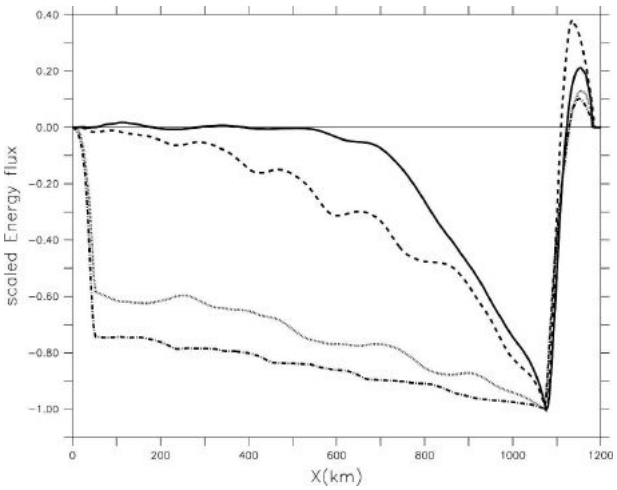


FIG. 17. The scaled energy flux of the internal tide (inward positive). The dash–dotted curve (without rotation) and dotted curve (with rotation) show the frictional decay of the energy transport in the case of a flat bottom. The dashed curve (without rotation) and solid curve (with rotation) show stronger trapping of internal tidal energy near the continental slope when the cross-channel bottom profile is parabolic.

Figure 17 still shows some oscillations in the along-channel direction, although these oscillations would have been much larger when heaving was not removed (Lu et al. 2001). The oscillations grow in time and should be attributed to the interference of the outward-propagating waves with reflected, inward-propagating waves. As was discussed in section 4, for each run a compromise in runtime had to be found, allowing the wave field to develop in time, but at the same time minimizing reflection from the open boundary sponge layer. The overall runtime length, however, has hardly any impact on the shape of the energy transport curves displayed in Fig. 17. Increasing the runtime (slightly) increases the absolute values of the transport curve, with decreasing amounts when the runtime becomes larger, but most prominently increases the oscillations on the energy transport curve. The difference in along-channel penetration of the energy transport between flat-bottom and sloping-bottom runs does not change anymore after runtimes of 4 days or longer.

Any decrease in energy transport must be associated with energy dissipation. As the sloping-bottom runs featuring geometric trapping show a much larger decrease in energy transport than the flat-bottom runs, the simulations that feature trapping should be subject to much larger energy dissipation. To be consistent with Fig. 17 we scale the energy dissipation in each run with its maximum (oceanward) energy transport. Figure 18 displays the energy dissipation in nondimensional units for the runs with rotation included. It is evident that the dissipation is much larger in the sloping-bottom run and that the dissipation is maximal near the continental slope and along the cross-channel slope where the right-bound Kelvin wave generates internal tides. We have tried to estimate whether the dissipation can be related to high-frequency motions by calculating a residual amplitude from the difference between the full-field variables and the sum of the harmonic amplitudes associated with the frequencies ranging from $\omega/2$ to $2\omega$, but this appeared not to be the case. In hindsight, this result is not surprising as the signature of trapping is prominent at the tidal-forcing frequency, and is associated with small-scale variations in wave energy (see Fig. 4). The implication of this is that when trapping occurs, even low-frequency motion leads to small spatial scales and subsequently to enhanced mixing.

## 6. Discussion and conclusions

### *a. Discussion*

In the present study we have discussed results for a very specific value of the lumped parameter $\tau$ ($\tau$ = 0.94), using an unrealistically small-amplitude barotropic tide to ensure a linear internal wave field response. This prompts the question of how general the findings are that we discuss. Both a systematic analysis of the effects of nonlinearities, as well as an analysis of the dependence of the results on the parameter $\tau$—after all *fractal* in the inviscid, analytical 2D case (Maas and Lam 1995)—justify a complete study of their own, which is beyond the scope of the present paper. However, we feel the need to briefly address these issues, in order to comment on the robustness of the results presented above for different parameter settings. Figure 19 shows the scaled energy flux of the internal tide for the trapped solution shown in Fig. 17 (with rotation on and a parabolic bottom profile), but now with a barotropic tide having a 100 times larger amplitude. The amplitude of the internal tide becomes a few meters instead of a few centimeters. We conclude from Fig. 19 that the scaled energy flux is very similar to the small-amplitude solution shown in Fig. 17. Nonlinear effects do not appear to affect the trapping of the internal wave field, which is determined by the slope of the bottom and the inclination of the beams. We do see some enhanced reflections near the open boundary, which can be explained by the reduced performance of the linear radiation condition for higher-amplitude internal waves.

Figure 19 also shows the effect of trapping for $\tau$ values that differ from the "optimal" value, $\tau$ = 0.94. According to 2D theory, the trapping regime of the simplest attractor is delimited by $\tau$ values of nearly 0.87 and 1. In that theory, outside this regime one finds

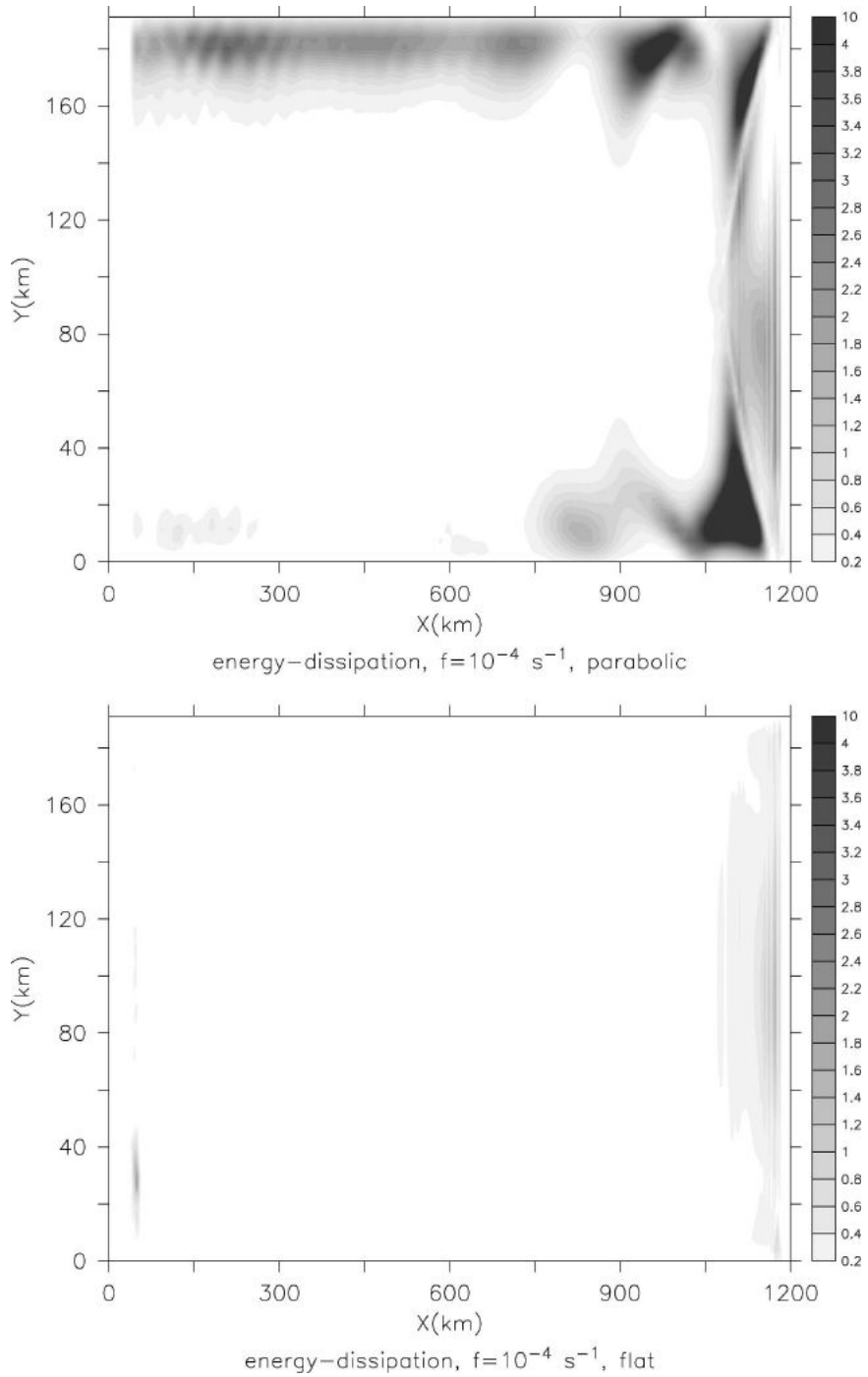


FIG. 18. The scaled, vertically integrated energy dissipation for the runs with rotation on. (top) The sloping-bottom case and (bottom) the flat-bottom case. Energy dissipation is scaled with maximum energy transport to explain the different decrease in outward transport. It is shown that trapping is associated with enhanced dissipation levels.

regimes with very geometrically complicated attractors, which would be reached after many more boundary reflections, presumably leading to less trapping to the continental slope. Although we have not explored the parameter range of $\tau$ exhaustively, our first results suggest that the 3D model exhibits a less discrete parameter sensitivity than the 2D theory predicts. In the 3D model, the range over which trapping occurs, seems to

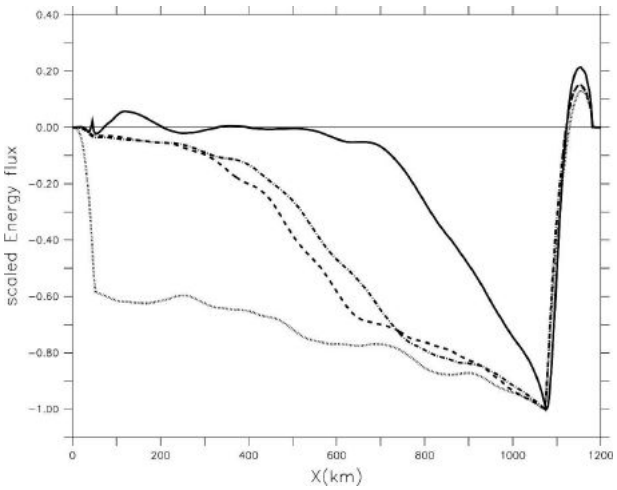


FIG. 19. The scaled energy flux (as in Fig. 17). The solid line is the trapped case with rotation in a parabolic channel, like in Fig. 17, but now with a 100 times larger forcing amplitude. The dashed and dash–dotted lines show trapping in the parabolic channel but for $\tau = 0.84$ and $\tau = 1.04$, respectively. The dotted line is the "untrapped," rotating flat-bottom case already shown in Fig. 17.

be wider and the transition from trapped to "untrapped" (free) solutions occurs more gradual. We show the energy flux for $\tau = 1.04$ and $\tau = 0.84$, having changed the channel width from 191.25 km to 172.5 and 210 km, respectively, keeping all other parameters constant. Figure 19 shows that trapping still occurs, but the penetration scale of the energy flux, measured in distance from the slope, has typically doubled with respect to that found for the optimal value, $\tau = 0.94$. This result emphasizes that trapping occurs over a distinct regime of parameter values and is not the result of a very specific parameter setting like the phenomenon of resonance. This implies that the results we have discussed show a certain robustness to parameter changes and might, when conditions are favorable, be detected in nature as well.

Circumstances in the (nearly parabolically shaped) Faeroe–Shetland Channel, north of Britain, in fact strongly suggest that internal tide penetration into the channel is severely restricted. Strong internal tides (baroclinic velocities of about 22 cm $s^{-1}$) are forced by tidal motions across the Wyville–Thomson ridge at the southern end of the Faeroe–Shetland Channel, where they are observed close to the ridge (Sherwin 1991). However, observations about 200 km to the northeast, in the down-channel direction, hardly contain any remaining internal tides (baroclinic amplitudes of about 5 cm $s^{-1}$; Hosegood and van Haren 2006). Recent field observations by a British–Dutch team (H. van Haren 2006, personal communication) reveal that, in between these two locations, at about 100 km from the ridge, moderate-amplitude internal tides (10 cm $s^{-1}$) can still be discerned. While the stratification in this case is far from uniform (the weakly stratified upper and lower parts of the water column are separated by a pycnocline at about 500-m depth), all in all this suggests that the internal tides are trapped in the down-channel direction, possibly through the refractive trapping mechanism as discussed in the present study.

As mentioned in the introduction, other observations also bear evidence of the existence of a "leaking" edge wave. At the continental slope, this takes the form of a deep internal tide that seems to be trapped in the cross-slope direction while propagating in the along-slope direction. These waves were encountered in the vicinity of the concave critical line both in the Atlantic Ocean near the African continental slope (Horn and Meincke 1976), as well as in the Pacific off California (Lerczak et al. 2003). Puzzling, the latter observations showed offshore phase propagation of the cross-shore currents, however, without following an offshore internal beam. A closer look at the ray structure of the edge wave in Fig. 1b shows that it is periodic and that each wavelength comprises six reflections. The ones at the bottom comprise focusing and defocusing reflections. We expect that only the intensified, near-bottom parts of the ray, that follow focusing reflections, will be observable and responsible for the wave's bottom-trapped appearance and apparent cross-shore phase propagation. Recent additional observations confirm the occurrence of such trapped, intensive internal tides, in this case at a depth of 1200 m, near the critical concave line on the continental slope off Portugal in the eastern Atlantic (Dias 2006).

### *b. Conclusions*

It has been demonstrated that a wave attractor may occur in an isopycnic, primitive equation ocean general circulation model when applied to a uniformly stratified 3D channel having sloping sidewalls. The attractor lies in the cross-channel plane, leading to down-channel trapping of the internal tides and mixing. The attractor coexists with a leaky kind of edge wave, for which focusing reflections are compensated by defocusing reflections. The latter wave propagates down channel along the critical line that connects points where the cross-channel slope is identical to the slope of the wave rays. The net energy transport associated with internal tides has a much smaller along-channel penetration when trapping occurs, which is associated with enhanced energy dissipation and mixing. Trapped solutions feature a much more finescale structure than the flat-bottom cases where the internal tide propagates

outward almost unimpeded. In the case of rotation, a marked asymmetry between the right- and left-bound edge wave occurs, with the right-bound edge wave being much more energetic. The reflected, barotropic right-bound Kelvin wave acts as a secondary internal wave generator along the cross-channel slope that feeds this internal edge wave.

*Acknowledgments.* We are grateful to Hans van Haren and the British–Dutch research team for sharing unpublished data on the internal tides in the Faeroe–Shetland Channel. We thank Margriet Hiehle for graphically processing some of the figures. We also thank two anonymous reviewers for their constructive comments.

## REFERENCES

Azevedo, A., J. C. B. da Silva, and A. L. New, 2006: On the generation and propagation of internal solitary waves in the southern Bay of Biscay. *Deep-Sea Res. I,* **53,** 927–941.

Baines, P. G., 1982: On internal tide generation models. *Deep-Sea Res.,* **29,** 307–338.

Bleck, R., and D. B. Boudra, 1981: Initial testing of a numerical ocean circulation model using a hybrid (quasi-isopycnic) vertical coordinate. *J. Phys. Oceanogr.,* **11,** 755–770.

——, and L. T. Smith, 1990: A wind-driven isopycnic coordinate model of the north and equatorial Atlantic Ocean. 1. Model development and supporting experiments. *J. Geophys. Res.,* **95,** 3273–3285.

Dias, J., 2006: Internal tide spatial variability off western Portugal detected by current meter observations. *Geophys. Res. Lett.,* **33,** L06613, doi:10.1029/2005GL024957.

Drijfhout, S. S., 2003: Why anticyclones can split. *J. Phys. Oceanogr.,* **33,** 1579–1591.

——, C. A. Katsman, L. de Steur, P. C. F. van der Vaart, P. J. van Leeuwen, and C. Veth, 2003: Modeling the initial, fast sea-surface height decay of Agulhas ring "Astrid." *Deep-Sea Res. II,* **50,** 299–319.

Egbert, G. D., and R. D. Ray, 2001: Estimates of $M_2$ tidal energy dissipation from TOPEX/Poseidon altimeter data. *J. Geophys. Res.,* **106,** 22 475–22 502.

Flather, R. A., 1988: A numerical model investigation of tides and diurnal-period continental shelf waves along Vancouver Island. *J. Phys. Oceanogr.,* **18,** 115–139.

Garrett, C. J. R., and W. H. Munk, 1972: Space-time scales of internal waves. *Geophys. Astrophys. Fluid Dyn.,* **3,** 225–264.

Gerkema, T., F.-P. A. Lam, and L. R. M. Maas, 2004: Internal tides in the Bay of Biscay: Conversion rates and seasonal effects. *Deep-Sea Res. II,* **51,** 2995–3008.

Gill, A. E., 1982: *Atmosphere–Ocean Dynamics.* Academic Press, 662 pp.

Holloway, P. E., 1996: A numerical model of internal tides with application to the Australian North West Shelf. *J. Phys. Oceanogr.,* **26,** 21–37.

——, and M. A. Merrifield, 1999: Internal tide generation by seamounts, ridges, and islands. *J. Geophys. Res.,* **104,** 25 937–25 952.

Horn, W., and J. Meincke, 1976: Note on the tidal current field in the continental slope area of Northwest Africa. *Memo. Soc. Roy. Sci. Liege,* **6** (10), 31–42.

Hosegood, P., and H. van Haren, 2006: Sub-inertial modulation of semi-diurnal currents over the continental slope in the Faeroe-Shetland Channel. *Deep-Sea Res. I,* **53,** 627–655.

Lam, F.-P. A., L. R. M. Maas, and T. Gerkema, 2004: Spatial structure of tidal and residual currents as observed over the shelf break in the Bay of Biscay. *Deep-Sea Res. I,* **51,** 1075–1096.

LeBlond, P. H., and L. A. Mysak, 1978: *Waves in the Ocean.* Elsevier, 602 pp.

Le Cann, B., 1990: Barotropic tidal dynamics of the Bay of Biscay shelf: Observations, numerical modelling and physical interpretation. *Cont. Shelf Res.,* **10,** 723–758.

Lerczak, J. A., C. D. Winant, and M. C. Hendershott, 2003: Observations of the semidiurnal internal tide on the southern California slope and shelf. *J. Geophys. Res.,* **108,** 3068, doi:10.1029/2001JC001128.

Lu, Y., D. G. Wright, and D. Brickman, 2001: Internal tide generation over topography: Experiments with a free-surface $z$-level ocean model. *J. Atmos. Oceanic Technol.,* **18,** 1076–1091.

Maas, L. R. M., 2001: Wave focusing and ensuing mean flow due to symmetry breaking in rotating fluids. *J. Fluid Mech.,* **437,** 13–28.

——, 2005: Wave attractors: Linear yet nonlinear. *Int. J. Bifurcation Chaos,* **15,** 2757–2782.

——, and F.-P. A. Lam, 1995: Geometric focusing of internal waves. *J. Fluid Mech.,* **300,** 1–41.

——, D. Benielli, J. Sommeria, and F.-P. A. Lam, 1997: Observation of an internal wave attractor in a confined, stably stratified fluid. *Nature,* **388,** 557–561.

Manders, A. M. M., and L. R. M. Maas, 2003: Observations of inertial waves in a rectangular basin with one sloping boundary. *J. Fluid Mech.,* **493,** 59–88.

——, and ——, 2004: On the three-dimensional structure of the inertial wave field in a rectangular basin with one sloping boundary. *Fluid Dyn. Res.,* **35,** 1–21.

Morozov, E. G., 1995: Semidiurnal internal wave global field. *Deep-Sea Res. I,* **42,** 135–148.

Müller, P., and X. Liu, 2000: Scattering of internal waves at finite topography in two dimensions. Part II: Spectral calculations and boundary mixing. *J. Phys. Oceanogr.,* **30,** 550–563.

Munk, W., and C. Wunsch, 1998: Abyssal recipes II: Energetics of tidal and wind mixing. *Deep-Sea Res. I,* **45,** 1977–2010.

New, A. L., 1988: Internal tidal mixing in the Bay of Biscay. *Deep-Sea Res.,* **35,** 691–709.

Ogilvie, G. I., and D. N. C. Lin, 2004: Tidal dissipation in rotating giant planets. *Astrophys. J.,* **610,** 477–509.

Orlanski, I., 1976: A simple boundary condition for unbounded hyperbolic flows. *J. Comput. Phys.,* **21,** 251–269.

Phillips, O. M., 1963: Energy transfer in rotating fluids by reflection of inertial waves. *Phys. Fluids,* **6,** 513–520.

——, 1977: *The Dynamics of the Upper Ocean.* 2d ed. Cambridge University Press, 336 pp.

Pingree, R. D., and A. L. New, 1989: Downward propagation of internal tidal energy into the Bay of Biscay. *Deep-Sea Res.,* **36,** 735–758.

——, and ——, 1991: Abyssal penetration and bottom reflection of internal tidal energy in the Bay of Biscay. *J. Phys. Oceanogr.,* **21,** 28–39.

Polzin, K. L., J. M. Toole, J. R. Ledwell, and R. W. Schmitt, 1997:

Spatial variability of turbulent mixing in the abyssal ocean. *Science,* **276,** 93–96.

Ray, R., and G. T. Mitchum, 1997: Surface manifestation of internal tides in the deep ocean: Observations from altimetry and island gauges. *Prog. Oceanogr.,* **40,** 135–162.

Raymond, W. H., and H. L. Kuo, 1984: A radiation boundary condition for multidimensional flows. *Quart. J. Roy. Meteor. Soc.,* **110,** 535–551.

Rieutord, M., B. Georgeot, and L. Valdettaro, 2001: Inertial waves in a rotating spherical shell: Attractors and asymptotic spectrum. *J. Fluid Mech.,* **435,** 103–144.

Sherwin, T. J., 1991: Evidence of a deep internal tide in the Faeroe Shetland channel. *Tidal Hydrodynamics,* B. B. Parker, Ed., Wiley and Sons, 469–488.

St. Laurent, L. C., and C. Garrett, 2002: The role of internal tides in mixing the deep ocean. *J. Phys. Oceanogr.,* **32,** 2882–2899.

——, H. L. Simmons, and S. R. Jayne, 2002: Estimating tidally driven mixing in the deep ocean. *Geophys. Res. Lett.,* **29,** 2106, doi:10.1029/2002GL015633.

Wunsch, C., and R. Ferrari, 2004: Vertical mixing, energy, and the general circulation of the oceans. *Annu. Rev. Fluid Mech.,* **36,** 281–314.